September 1985 LRP 268/85

TEXTBOOK FINITE ELEMENT METHODS APPLIED TO LINEAR WAVE PROPAGATION PROBLEMS INVOLVING CONVERSION AND ABSORPTION

K. Appert, T. Hellsten, J. Vaclavik and L. Villard

Paper presented at the

3rd European Workshop on Problems in the Numerical Modeling of Plasmas
NUMOP 85

Varenna, Italy, 10 - 13 September 1985

TEXTBOOK FINITE ELEMENT METHODS APPLIED TO LINEAR WAVE PROPAGATION PROBLEMS INVOLVING CONVERSION AND ABSORPTION

K. Appert, T. Hellsten*, J. Vaclavik and L. Villard

Centre de Recherches en Physique des Plasmas
Association EURATOM - Confédération Suisse
Ecole Polytechnique Fédérale de Lausanne
21, Av. des Bains, CH-1007 Lausanne, Switzerland

* JET-Joint Undertaking, Abingdon, Oxfordshire, United Kingdom

ABSTRACT

A system of two second order ordinary differential equations describing wave propagation in a hot plasma is solved numerically by the finite element method involving standard linear and cubic elements. Evanescent short-wavelength modes do not constitute a problem because of the variational nature of the method. It is straightforward to generalize the method to systems of equations with more than two equations. The performance of the method is demonstrated on known physical situations and is measured by investigating the convergence properties. Cubic elements perform much better than linear ones. In an application it is shown that global plasma oscillations might have an importance for the linear wave conversion in the ion-cyclotron range of frequency.

1. INTRODUCTION

The present study is motivated by fusion research. It is, however, believed that the mathematical problem discussed here is of sufficiently general nature to be interesting to readers outside the fusion community as well. The problem is of a deceivingly simple nature: solving a system of two linear ordinary second order differential equations with non-constant complex coefficients.

The system of equations which we shall discuss will be taken from the theory of plasma heating by waves in the ion-cyclotron range of frequency, ICRF [1]. Equations of very similar nature would, however, be obtained for the heating of inhomogeneous plasmas by any other wave, the two extreme cases being Alfvén Wave Heating [2] at low frequency and laser-plasma interaction [3] at extremely high frequency. The equations are obtained from Maxwell's equations under the ansatz $\exp(-i\omega t)$ where ω is the imposed frequency. In all cases, the two coupled second order differential equations in space x describe two linearly-coupled wave branches which can be called the slow and the fast wave. Each branch consists of one left and one right-running damped or evanescent wave - depending on parameters and spatial location.

In general, the two wave branches have quite different wavelengths or, equivalently, damping lengths. In mathematical terms the system is stiff. While only a few wavelengths of the fast wave might fit into the solution domain (the plasma cross-section!), hundreds of wavelengths of the slow wave are needed to span it. This does, however, not mean that the wave form will necessarily exhibit the slow-wave fine structure

throughout the whole plasma volume, because the slow wave is generated by mode conversion at specific points and is subsequently damped as it propagates away from these points. This scenario is typical for many radio-frequency heating schemes and also for laser-plasma interaction. The external coupler (antenna, wave-guide, laser cavity) excites the fast wave which transports energy towards the plasma centre. If the inhomogeneities have the effect that the wavelengths of the fast and the slow waves are comparable at specific points in space, energy can be exchanged between the fast and the slow waves in the neighbourhood of these points. This phenomenon is called mode conversion.

In a case, as just described, a straightforward numerical integration (initial value approach or "shooting" approach) is usually impossible [4], because the small-scale (partly evanescent) wave which propagates against the direction of integration is "generated" from numerical noise and appears as an exponentially growing solution (in the direction of integration). The unphysical, exponentially-growing part dominates the real physics and makes it disappear in the round-off errors long before the integration procedure has reached the other end of the domain.

There are, broadly speaking, two numerical methods which allow to tackle the problem with success. One only is extensively used by the plasma RF community [5,6,7,8,9], the other will be described in the present paper. The first method can best be characterised by saying that it uses some analytical results as an essential ingredient, e.g. slicing up the plasma into different regions where different approximations may hold and matching the solutions across the interfaces. The

second method consists of a straightforward discretisation of the differential equations in the whole plasma region and a search for a global (or instantaneous) solution to the boundary value problem as it has been used in calculations for Alfvén Wave Heating [2]. Both methods have their advantage and their disadvantage. The first method makes good use of computer space but is not very modular in the sense that it is not easy to change the physics. Each change in physics must be preceded by the pertinent analysis. Conversely, the second method makes it easy to change the physics but needs more computer space, at least in its most primitive form.

2. FORMULATION OF THE PHYSICAL PROBLEM

In simple models of plasma heating by waves in the ion-cyclotron range of frequency, one adopts usually a plane geometry. Specifally, we adopt the geometry shown in Fig. 1. The extension of the arrangement is infinite in the ignorable directions y and z. The plasma is situated in the domain $x_{pl} \leq x \leq x_{pr}$, and is inhomogeneous along x. On both sides it is separated from an ideally conducting wall by vacuum regions (III: $x_{sl} < x < x_{pl}$ and II: $x_{pr} < x < x_a$, I: $x_a < x < x_{sr}$). An antenna is placed into the vacuum on the right side at $x = x_a$. Since this investigation is restricted to linear wave propagation in a steady state, all the wave quantities can be assumed to vary as $\exp[i(k_y y + k_z z - \omega t)]$. The goal is to determine the dependence of the wave field on x.

2.1 Wave equation in the plasma

In the plasma the wave field is described by equations similar to those of Colestock and Kashuba [5], Swanson [12] and Chiu and Mau [8] except that we assume the electric field parallel to the magnetic field to vanish, i.e. $\vec{E} = (E_x, E_y)$. The effects of electron Landau damping of the ion Bernstein wave are simulated by a phenomenological damping coefficient ν. The equations written in compact form are

$$\mathrm{rot}\,\mathrm{rot}\,\vec{E} = \left[\vec{\vec{\varepsilon}} - \frac{\partial}{\partial x}\vec{\vec{\alpha}}_x \frac{\partial}{\partial x} + k_y^2 \vec{\vec{\alpha}}_y\right]\vec{E}\,, \tag{1}$$

where

$$\left.\begin{aligned} \vec{\vec{\varepsilon}} &= \begin{pmatrix} \varepsilon_\perp & \varepsilon_{xy} \\ -\varepsilon_{xy} & \varepsilon_\perp \end{pmatrix}, \\ \varepsilon_\perp &= \sum_\ell \kappa_\ell \left(Z_1^{(\ell)} + Z_{-1}^{(\ell)}\right), \\ \varepsilon_{xy} &= i\sum_\ell \kappa_\ell \left(Z_1^{(\ell)} - Z_{-1}^{(\ell)}\right) - i\frac{\omega_{pe}^2\,\omega}{\omega_{ce}\,c^2}\,, \end{aligned}\right\} \tag{2}$$

$$
\left.
\begin{aligned}
&\overrightarrow{\overrightarrow{\alpha}}_x = \begin{pmatrix} \alpha_1 & \alpha_3 \\ -\alpha_3 & \alpha_2 \end{pmatrix}, \qquad \overrightarrow{\overrightarrow{\alpha}}_y = \begin{pmatrix} \alpha_2 & \alpha_3 \\ -\alpha_3 & \alpha_1 \end{pmatrix}, \\
&\alpha_1 = \sum_\ell \tau_\ell \left[Z_2^{(\ell)} + Z_{-2}^{(\ell)} - Z_1^{(\ell)} - Z_{-1}^{(\ell)} \right] + i\nu , \\
&\alpha_2 = \sum_\ell \tau_\ell \left[Z_2^{(\ell)} + Z_{-2}^{(\ell)} - 3\left(Z_1^{(\ell)} + Z_{-1}^{(\ell)} \right) + 4 Z_0^{(\ell)} \right], \\
&\alpha_3 = i \sum_\ell \tau_\ell \left[Z_2^{(\ell)} - Z_{-2}^{(\ell)} - 2\left(Z_1^{(\ell)} - Z_{-1}^{(\ell)} \right) \right],
\end{aligned}
\right\} \qquad (3)
$$

and

$$
\left.
\begin{aligned}
&\tau_\ell = \kappa_\ell \rho_\ell^2 = \frac{\omega\, \omega_{p\ell}^2\, v_{th\ell}}{4 c^2 k_z\, \omega_{c\ell}^2} , \\
&\kappa_\ell = \frac{\omega\, \omega_{p\ell}^2}{2 c^2 k_z\, v_{th\ell}} , \\
&Z_m^{(\ell)} = Z\left(\frac{\omega - m\omega_{c\ell}}{k_z\, v_{th\ell}} \right) .
\end{aligned}
\right\} \qquad (4)
$$

Here, summation extends over all ion species ℓ; Z denotes the complex-valued Fried-Conte dispersion function [13], $v_{th\ell}$, $\omega_{p\ell}$ and $\omega_{c\ell}$ are the thermal velocity, plasma frequency and cyclotron frequency respectively of the ℓth species.

The dielectric tensor in eq. (1) (the square bracket) has been obtained with the following procedure. The dielectric tensor for a homo-

geneous hot plasma [14] has been expanded up to second order in $k_\perp \rho_\ell$ where ρ_ℓ denotes the ion Larmor radius and $\vec{k}_\perp = (k_x, k_y)$. Then ik_x is replaced by ∂/∂_x and a form of eq. (1) is sought which satisfies energy conservation. Some of the terms containing ∂/∂_x on the right-hand side can be placed in an unambiguous way. These are the terms appearing in eq. (1). Other terms cannot be placed unambiguously. Those terms are discarded. Despite of the dubious derivation, eq. (1) can be regarded as a reasonable model for wave propagation in the ion-cyclotron range of frequencies. The equation is presently subject to some discussion in the community [5,8,12,15,16].

2.2 Wave equations in the vacuum and conditions at interfaces

The wave field in the vacuum is given by Maxwell's equations neglecting the displacement current: the wave is treated as an evanescent wave. It obeys the equation

$$\frac{d^2 B_z}{dx^2} - \kappa^2 B_z = 0 , \tag{5}$$

where $\kappa^2 = k_y^2 + k_z^2$. The general solution obviously is

$$B_z = C_1 e^{\kappa x} + C_2 e^{-\kappa x} \tag{6}$$

with C_1 and C_2 being constants.

The particular solution in plasma and vacuum is obtained by imposing the pertinent conditions at the five interfaces x_{sl}, x_{pl}, x_{pr}, x_a and x_{sr}. This procedure is somewhat cumbersome but unavoidable. The condition at $x = x_{sl}, x_{sr}$ is:

$$B_z' = 0 . \tag{7}$$

The prime denotes the derivative d/dx. Assuming a divergence-free current distribution on the antenna

$$\vec{j} = i\,\delta(x - x_a)\,\vec{e}_x \times \nabla\beta \tag{8}$$

one obtains from Maxwell's equations the conditions [10,11]

$$[\![B_z]\!] = -(4\pi/c)\,k_z\,\beta , \tag{9}$$

$$[\![B_z']\!] = 0 \tag{10}$$

at $x = x_a$. Here $[\![B]\!] = B|_{\text{outside}} - B|_{\text{inside}}$ and $\vec{e}_x$ denotes the unit vector in x direction and $\beta = \beta_0 \exp[i(k_y y + k_z z - \omega t)]$, $\beta_0 = \text{const}$. This quantity can be called the "current potential"; it is the source of the wave field.

The matching conditions at the plasma-vacuum interfaces $x = x_{pl}, x_{pr}$ are partly given by $\text{rot}\,\vec{E} = -(1/c)\vec{B}$ from which we conclude that

$$[\![E_y]\!] = 0 \tag{11}$$

and

$$[\![E_z]\!] = 0 . \tag{12}$$

The latter condition is just $E_z = 0$ on the plasma surface because it has been assumed that $E_z = 0$ everywhere inside the plasma. Two additional conditions are needed and they can be obtained by integrating eq. (1) over an infinitesimally small boundary layer assuming finite temperature (α_i finite) inside and zero temperature ($\alpha_i = 0$) outside this layer. We find

$$\alpha_1 E_x' + \alpha_3 E_y' \Big|_{inside} = 0 , \tag{13}$$

and

$$\alpha_3 E_x' - \alpha_2 E_y' \Big|_{inside} = [\![E_y' - ik_y E_x]\!] . \tag{14}$$

Using eq. (12) and Maxwell's equations, the electric field $\vec{E}|_{outside}$ in eqs. (11) and (13) can be replaced by the magnetic field:

$$k_z^2 E_y = (i\omega/c) B_z' , \tag{15}$$

$$-ik_y E_x + \alpha_3 E_x' + (1-\alpha_2) E_y' = (i\omega/c) B_z . \tag{16}$$

Discussing the plasma-vacuum interface, from now on we mean by $\vec{E}$ the field just inside the interface and, in contrast, by $\vec{B}$ the field just outside.

The aim is to derive two linear relations between B_z and B_z' (one per plasma-vacuum interface) using all the knowledge concerning the solution in the vacuum regions. Making use of eqs. (15) and (16),

one will then obtain two boundary conditions which, together with eq. (1), determine the solution in the plasma.

For the left plasma surface, $x = x_{pl}$, we find from eqs. (6) and (7)

$$\left\{ \kappa \tanh[\kappa (x_{pl} - x_{sl})]\, B_z - B_z' \right\}_{x = x_{pl}} = 0. \qquad (17)$$

For the right side, it is convenient to search first an expression for the field in region I

$$B_z(x) = C_0' \left\{ \exp[\kappa (x - x_{sr})] + \exp[-\kappa (x - x_{sr})] \right\}, \qquad (18)$$

and in region II

$$B_z(x) = C_1' \exp(\kappa x) + C_2' (-\kappa x). \qquad (19)$$

The coefficient C_0 is so far an undetermined constant, whereas the coefficients C_1 and C_2 can be expressed in terms of B_z and B_z' at $x = x_{pr}$:

$$\left.\begin{aligned} C_1' &= \frac{1}{2} \left(B_z + \frac{1}{\kappa} B_z' \right)_{x = x_{pr}} \exp(-\kappa x_{pr}), \\ C_2' &= \frac{1}{2} \left(B_z - \frac{1}{\kappa} B_z' \right)_{x = x_{pr}} \exp(\kappa x_{pr}). \end{aligned}\right\} \qquad (20)$$

The two solutions, eqs. (18) and (19), can now be matched across the

antenna using eqs. (9) and (10). The result is:

$$\left\{ \kappa \tanh\left[\kappa(x_{pr}-x_{sr})\right] B_z - B_z' \right\}_{x=x_{pr}} = \mathcal{S} , \qquad (21)$$

with the source term

$$\mathcal{S} = -(4\pi/c)\,\kappa k_z \beta_0 \sinh\left[\kappa(x_{sr}-x_a)\right] / \cosh\left[\kappa(x_{sr}-x_{pr})\right] . \qquad (22)$$

Equations (17) and (21) are the two desired linear relations between B_z and B_z'. They can be transformed into relations for the electric fields inside the plasma-vacuum interface by means of eqs. (14), (15) and (16). At the left interface, $x = x_{pl}$, we have

$$(D/\alpha_1) E_y' = -ik_y E_x - (k_z^2/\kappa) \coth\left[\kappa(x_{pl}-x_{sl})\right] E_y , \qquad (23)$$

and on the right side, $x = x_{pr}$,

$$(D/\alpha_1) E_y' = -ik_y E_x + (k_z^2/\kappa) \coth\left[\kappa(x_{sr}-x_{pr})\right] E_y + \frac{i\omega}{\kappa c} \mathcal{S} \coth\left[\kappa(x_{sr}-x_{pr})\right] , \qquad (24)$$

where $D = \alpha_3^2 + \alpha_1(\alpha_2-1)$.

These two boundary conditions together with the two conditions given by eq. (13) determine a unique solution of eq. (1).

Here a remark concerning the present section is in order. For those readers who are just interested in the mathematical problem of a wave conversion process, this section might appear unnecessarily long. He might be tempted to believe that arbitrarily chosen boundary conditions would be sufficient for a discussion of the solutions of eq. (1). This is, however, not true. In general, there is a severe boundary layer problem if the wave field does not satisfy eqs. (13) and (14) at the boundary. The additional material presented can serve for the design of antenna and generator circuits. In this context there is particular interest in the relation between the current, eq. (8), flowing in the antenna and the amplitude of the wave field in the plasma, and the complex power per area emitted by the antenna [10,11],

$$P/A = -\frac{1}{2}\int_{x_a-0}^{x_a+0} \vec{j}\cdot\vec{E}^{*}\,dx \quad . \tag{25}$$

Using Maxwell's equations and eq. (8), one finds $P/A = (i\beta\omega/2ck_z)$ $*dB_z^*/dx$ at $x = x_a$. From this and eqs. (19) and (20) it follows then

$$P/A = \frac{i\beta\omega\kappa}{2ck_z}\left\{B_z^{*}\sinh[\kappa(x_a-x_{pr})] + \frac{1}{\kappa}\frac{dB_z^{*}}{dx}\cosh[\kappa(x_a-x_{pr})]\right\}_{x=x_{pr}} . \tag{26}$$

Once the solution in the plasma is found, the power can then be expressed in terms of E_y at the inside of the plasma vacuum interface using eqs. (13), (15), (16) and (24).

2.3 Variational form

The finite element method is usually applied to a variational form of the differential equations to be solved. In the case of equations describing a dissipative system, like ours, only a weak (Galerkin) variational form can be constructed. Let $G(x) = (G_x(x), G_y(y)) * \exp[i(k_y y + k_z z - \omega t)]$ be an arbitrary test function in some functional space of sufficient regularity; in particular dG/dx must exist. The weak form is obtained by multiplying eq. (1) by G^* and integrating over the plasma domain. After the partial integration of the terms containing second derivatives one has

$$\int_{x_{pl}}^{x_{pr}} \left[\vec{G}^* \cdot \left(\vec{\vec{\varepsilon}} + k_y^2 \vec{\vec{\alpha}}_y \right) \cdot \vec{E} + \frac{\partial \vec{G}^*}{\partial x} \cdot \vec{\vec{\alpha}}_x \cdot \frac{\partial \vec{E}}{\partial x} - \mathrm{rot}\, \vec{G}^* \cdot \mathrm{rot}\, \vec{E} \right] dx = T(x_{pr}) - T(x_{pl}) \,, \quad (27)$$

where

$$T = \vec{G}^* \cdot \vec{\vec{\alpha}}_x \cdot \frac{\partial \vec{E}}{\partial x} - \left(\vec{G}^* \times \mathrm{rot}\, \vec{E} \right) \cdot \vec{e}_x \quad (28)$$

Equations (27) and (28) hold for an arbitrary choice of $\vec{G}$. The boundary conditions eqs. (13), (23) and (24) are natural conditions and are enforced by using them in T:

$$T(x_{pl}) = G_y^* \left\{ -(k_z^2/\kappa) \coth\left[\kappa(x_{pl} - x_{sl})\right] E_y \right\} \Big|_{x = x_{pl}} \,, \quad (29)$$

$$T(x_{pr}) = G_y^* \left\{ \frac{k_z^2}{\kappa} \coth[\kappa(x_{sr}-x_{pr})] E_y + \frac{i\omega}{\kappa c} \Delta \coth[\kappa(x_{sr}-x_{pr})] \right\} \Big|_{x=x_{pr}} . \qquad (30)$$

It is this form of eq. (27) which, in the next chapter, will be discretised.

Here it remains to be mentioned that with $G^* = (ic^2/8\pi\omega)E^*$, the differential form of eq. (27) is an energy conservation law:

$$Q + dS_x/dx = 0. \qquad (31)$$

The energy density absorbed per second Q is given by

$$Q = Im \frac{c^2}{8\pi\omega} \left[\vec{E}^* \cdot \left(\vec{\vec{\varepsilon}} + k_y^2 \vec{\vec{\alpha}}_y \right) \cdot \vec{E} + \frac{\partial \vec{E}^*}{\partial x} \cdot \vec{\vec{\alpha}}_x \cdot \frac{\partial \vec{E}}{\partial x} \right] \qquad (32)$$

and the x-component of the energy flux by

$$S_x = Im \frac{c^2}{8\pi\omega} \left[E_y^* \left(\frac{\partial E_y}{\partial x} - ik_y E_x \right) - \vec{E}^* \cdot \vec{\vec{\alpha}}_x \cdot \frac{\partial \vec{E}}{\partial x} \right]. \qquad (33)$$

The first term in eq. (33) represents the Poynting flux, i.e. the energy transported by the electromagnetic field, whereas the second term must be ascribed to the particles; it is the kinetic energy flux accompanying a slow wave. Equation (31) can be used as a first check of the computer code. In particular the flux S_x must be equal to the real part of the power emitted by the antenna, eq. (26).

3. FINITE ELEMENT DISCRETISATION

3.1 Mesh and basis functions

As already suggested by the title of the present study, the discretisation of eq. (27) can be achieved with the standard methods [11,17,18 19]. Let us define an arbitrary non-equidistant, spatial mesh by

$$x_{pl} \equiv x_0 < x_1 < \cdots < x_j < \cdots < x_N \equiv x_{pr} \,. \tag{34}$$

A finite element approximation to the solutions of eq. (27) is obtained by using piecewise polynomials for the functions $E_x(x)$, $E_y(x)$, $G_x(x)$ and $G_y(x)$. The simplest possible approximation is by piecewise linear functions (linear finite elements). The existence of the first derivative is sufficient to make eq. (27) meaningful. It does indeed not matter that the first derivative is not continuous. As we shall see in the remainder of this paper, with linear elements it is not easy to achieve good convergence properties for the interesting physical situations. For this reason, we discuss the discretisation with linear and cubic Hermite finite elements. The cubic Hermites engender an approximation where the approximated function and its first derivative are continuous across a nodal point x_j.

Let $U(x)$ be the function to be approximated by finite elements in the range $x_0 \leq x \leq x_N$. The expansion in terms of linear finite elements is given by

$$U(x) = \sum_{j=0}^{N} u^j \sigma_j(x) \,, \tag{35}$$

where

$$\sigma_j(x) = \begin{cases} 0 & x \leq x_{j-1}, \\ \dfrac{x - x_{j-1}}{x_j - x_{j-1}}, & x_{j-1} \leq x \leq x_j, \\ \dfrac{x_{j+1} - x}{x_{j+1} - x_j}, & x_j \leq x \leq x_{j+1}, \\ 0, & x_{j+1} \leq x. \end{cases} \tag{36}$$

The linear basis function $\sigma_j(x)$ is depicted in Fig. 2 together with the two cubic basis functions, $\psi_j(x)$ and $\phi_j(x)$ needed for the higher order expansion;

$$U(x) = \sum_{j=0}^{N} \left(u^j \psi_j(x) + \rho^j \varphi_j(x) \right). \tag{37}$$

Here

$$\psi_j(x) = \begin{cases} 0, & x \leq x_{j-1}, \\ \sigma_j^2(x)\left[3 - 2\sigma_j(x)\right], & x_{j-1} \leq x \leq x_{j+1}, \\ 0, & x_{j+1} \leq x, \end{cases} \tag{38}$$

and

$$\varphi_j(x) = \begin{cases} 0 & , \quad x \leq x_{j-1} , \\ \sigma_j^2(x)\,(x - x_j) & , \quad x_{j-1} \leq x \leq x_{j+1} , \\ 0 & , \quad x_{j+1} \leq x . \end{cases} \tag{39}$$

Note that all these functions have a finite support (hence finite elements) and that $\sigma_j(x_i) = \delta_{ij}$, $\psi_j(x_i) = \delta_{ij}$, $\psi_j'(x_i) = 0$, $\phi_j(x_i) = 0$ and $\phi_j'(x_i) = \delta_{ij}$ where δ_{ij} is the Kronecker delta. From these relations follows that $U(x_j) = u_j$ and $U'(x_j) = p_j$.

Using the linear expansion, eq. (35), our variational problem, eq. (27), is reduced to the problem of determining the 2(N+1) expansion coefficients $u_1{}^j$ and $u_2{}^j$ of E_x and E_y. A system of linear equations for these unknowns can be obtained by letting the test function $\vec{G}^*$ or rather its components $G_x(x)$ and $G_y(x)$ run through the basis, eq. (36), j = 0,...,N. There is nothing arbitrary in the choice of $\vec{G}^*$ because any piecewise linear function can be expressed as U(x), eq. (35), or in other words, because the system of functions, eq. (36), is indeed a basis of the finite-dimensional function space in question (the space of piecewise linear functions). For the approximation by cubic functions, the procedure is analogous.

3.2 Compact form of variational problem

In order to be more explicit, let us write eq. (27) in a compact form:

$$\sum_{\mu,\nu=1}^{2}\sum_{\kappa\lambda=0}^{1}\int_{X_0}^{X_N} dx\,\frac{d^{\kappa}V_{\mu}^{*}}{dx^{\kappa}}\,C_{\kappa\lambda}^{\mu\nu}\,\frac{d^{\lambda}U_{\nu}}{dx^{\lambda}} = \sum_{\mu=1}^{2} V_{\mu}^{*}\left[\sum_{\nu=1}^{2} R^{\mu\nu}U_{\nu} + Z^{\mu}\right]\Bigg|_{X_0}^{X_N}. \qquad (40)$$

It is, by the way, for a general variational form of this type that we have developed the finite element software. The software does not depend on the specific physical problem discussed here in contrast with other methods used to study ICRF heating [5,6,8,9]. Our software is useful for every linear wave propagation problem which can be described by differential equations of arbitrary order.

By comparison of eqs. (27) and (40) using eqs. (29) and (30), it is easy to find the actual form of the quantities in eq. (40). First, U_ν and V_μ are defined by

$$\left.\begin{aligned}\vec{E} &= \left(U_1(x), U_2(x)\right)\exp\left[i\left(k_y y + k_z z - \omega t\right)\right],\\ \vec{G} &= \left(V_1(x), V_2(x)\right)\exp\left[i\left(k_y y + k_z z - \omega t\right)\right].\end{aligned}\right\} \qquad (41)$$

Further, all the coefficients $C_{\kappa\lambda}^{\mu\nu} = 0$ with the exception of

$$\left.\begin{aligned}&C_{11}^{11} = \alpha_1, \quad C_{11}^{12} = -C_{11}^{21} = \alpha_3, \quad C_{11}^{22} = \alpha_2 - 1,\\ &C_{01}^{12} = -C_{10}^{21} = -ik_y, \quad C_{00}^{11} = \varepsilon_\perp + k_y^2\alpha_2 - k_z^2 - k_y^2,\\ &C_{00}^{12} = -C_{00}^{21} = \varepsilon_{xy} + k_y^2\alpha_3, \quad C_{00}^{22} = \varepsilon_\perp + \alpha_1 k_y^2 - k_z^2.\end{aligned}\right\} \qquad (42)$$

The vertical bar on the right hand side of eq. (40) means that the difference between the expression evaluated at $x = x_N$ and at $x = x_O$ has to be taken. From equations (29) and (30) we find $R^{\mu\nu}(x) = Z^{\mu}(x) = 0$ with the exception of

$$\left.\begin{aligned} R^{22}(x_0) &= -\frac{k_z^2}{\kappa}\coth\left[\kappa(x_{pl}-x_{sl})\right], \\ R^{22}(x_N) &= \frac{k_z^2}{\kappa}\coth\left[\kappa(x_{sr}-x_{pr})\right], \\ Z^2(x_N) &= \frac{i\omega}{\kappa C}\,s\coth\left[\kappa(x_{sr}-x_{pr})\right]. \end{aligned}\right\} \qquad (43)$$

3.3 Discretized form of variational problem

We merely discuss the approximation by cubics which is a harder problem than the one by linear elements. The quantities U_ν and V_μ are expanded according to eq. (37),

$$\left.\begin{aligned} U_\nu &= \sum_{j=0}^{N}\left(u_\nu^j\,\psi_j + p_\nu^j\,\varphi_j\right), \\ V_\mu &= \sum_{j=0}^{N}\left(v_\mu^j\,\psi_j + q_\mu^j\,\varphi_j\right), \end{aligned}\right\} \qquad (44)$$

and inserted in eq. (40). Remember that V_μ is a test function supposed to take one by one all the 4(N+1) possible linearly independent values. The 4(N+1) choices are

$$\left[(v_\mu^i = 1,\ q_\mu^i = 0),\ (v_\mu^i = 0,\ q_\mu^i = 1),\ \mu = 1,2 \right],$$

$$\left[(v_\mu^i = 0,\ q_\mu^j = 0,\ \forall j \neq i),\ \mu = 1,2 \right],\quad i = 0, 1, \ldots, N. \tag{45}$$

Equation (40) then assumes the form.

$$\left.\begin{aligned} &\sum_{j=0}^{N} \sum_{\nu=1}^{2} \left(u_\nu^j H_{ij}^{\mu\nu} + p_\nu^j K_{ij}^{\mu\nu} \right) \\ &\qquad = \delta_{iN} \left[R^{22}(x_N) u_2^N + Z^2(x_N) \right] - \delta_{i0} R^{22}(x_0) u_2^0 , \\ &\sum_{j=0}^{N} \sum_{\nu=1}^{2} \left(u_\nu^j M_{ij}^{\nu\mu} + p_\nu^j N_{ij}^{\mu\nu} \right) = 0 , \quad \mu = 1,2 \text{ and } i = 0, \ldots, N \end{aligned}\right\} \tag{46}$$

where

$$\left.\begin{aligned} H_{ij}^{\mu\nu} &= \sum_{\kappa,\lambda=0}^{1} \int dx\ \frac{d^\kappa \psi_i}{dx^\kappa} C_{\kappa\lambda}^{\mu\nu} \frac{d^\lambda \psi_j}{dx^\lambda} , \\ K_{ij}^{\mu\nu} &= \sum_{\kappa,\lambda=0}^{1} \int dx\ \frac{d^\kappa \psi_i}{dx^\kappa} C_{\kappa\lambda}^{\mu\nu} \frac{d^\lambda \varphi_j}{dx^\lambda} . \end{aligned}\right\} \tag{47}$$

The matrices $M_{ij}^{\mu\nu}$ and $N_{ij}^{\mu\nu}$ have the form of $H_{ij}^{\mu\nu}$ and $K_{ij}^{\mu\nu}$ with ψ_i (and not ψ_j) replaced by ϕ_i. Equation (46) is a linear algebraic equation for the unknown vector (u_1^0, p_1^0, u_2^0, p_2^0, u_1^1, p_1^1,...., p_2^{N-1}, u_1^N, p_1^N, u_2^N, p_2^N). The matrix of this linear system has a band structure; the bandwidth is 15. The system can be solved by any standard method.

Those readers who did not get lost in the preceding forest of indices will find it easy to formulate the linear system for the unknown vector (u_1^0, u_2^0, u_1^1, u_2^1,...., u_2^N) in the case of an expansion in terms of linear functions, eq. (35). In this case, the bandwidth of the resulting matrix is 7.

4. BASIC PHYSICAL PHENOMENA

It might appear strange that the basic physical phenomena described by eq. (1) are presented before the convergence studies of the numerical scheme. It is, however, reasonable to test the convergence on physically relevant cases only and these have to be discussed first. As an example of what we call "physically doubtful" cases, we just mention those where the expansion in $k_\perp \rho_i$ leading to eqs. (1) to (4) breaks down. It is in these particular cases that the numerical resolution most likely is insufficient.

4.1 Energy conservation

As we have seen in eq. (31), the conservation of energy is a trivial consequence of the weak form, eq. (27). As we have described the weak form, the energy in the numerical model is exactly conserved provided Q and dS_x/dx are defined consistently in terms of finite elements, i.e. by writing

$$\int_{x_i}^{x_{i+1}} Q\,dx + S_x(x_{i+1}) - S_x(x_i) = 0$$

instead of eq. (31) and using the finite element expansions. Defined in this way the energy is conserved even if the resolution of the discretisation is insufficient for a meaningful physical result. Typing errors in the code can be detected in this way.

More information can be obtained from eq. (31) when a straightforward finite difference approximation is used for dS_x/dx:

$$\Delta_i = Q_i + \frac{(S_x)_{i+1} - (S_x)_{i-1}}{x_{i+1} - x_{i-1}} \,. \qquad (48)$$

In this local evaluation one uses the solution vector $(u_\nu^i,\ p_\nu^i)$ in the case of cubic elements and

$$\left(u_\nu^i,\ \frac{p_\nu^i - p_\nu^{i-1}}{x_i - x_{i-1}} \frac{x_{i+1} - x_i}{x_{i+1} - x_{i-1}} + \frac{p_\nu^{i+1} - p_\nu^i}{x_{i+1} - x_i} \frac{x_i - x_{i-1}}{x_{i+1} - x_{i-1}} \right)$$

in the case of linear elements. The magnitude of Δ_i relative to some typical value of Q_i is a measure for the quality of the resolution.

In Figure 3 are shown Q_i and Δ_i for a typical physically relevant case [1] obtained with cubic elements. The geometrical dimensions (see Fig. 1) of the plasma are: $x_{pr} = |x_{pl}| = 125$ cm, $x_a = 150$ cm, $x_{sr} = |x_{sl}| = 170$ cm and the major radius is $R = 296$ cm. The magnetic field has a value of 2.71 T at $x = 0$ and varies as $R/(R+x)$. The plasma consists of a mixture of 3 ion species D^+, T^+ and $^3He^{++}$ whose central densities are $4.5 \cdot 10^{13}$, $4.5 \cdot 10^{13}$ and $0.5 \cdot 10^{13}$ cm^{-3} respectively. The central ion and electron temperatures are 5 keV. The density profiles are parabolic and behave as $1.05-(x/170)^2$. The temperatures have the form $[1.1-(x(170)^2]^2$. The phenomenological damping $\nu = 10^{-4}$. The excitation parameters are the frequency $\omega/2\pi = 55.1$ MHz, and the wave numbers $k_y = 0.01$ and $k_z = 0.05$ cm^{-1}. The amplitude of the current potential is chosen throughout the paper $\beta_o = -i$. A non-equidistant mesh with $N = 500$ intervals has been used. The density of the mesh points is proportional to

$$1 + 5 \exp\left[-\frac{1}{2}\left(\frac{x+5}{15}\right)^2\right] + 3 \exp\left[-\frac{1}{2}\left(\frac{x+80}{10}\right)\right],$$

where x is in cm. We remark in Fig. 3 that the worst energy balance is obtained somewhat to the left of the two absorption peaks at $x = 0$ and $x = -74$ cm. From Fig. 3 we surmise that the resolution is not too good at these points. The result for the parameter

$$\zeta = \max_i \Delta_i \,/\, \max_i Q_i \tag{49}$$

is, however, acceptable; $\zeta = 0.031$.

That we have indeed a resolution problem can be shown most clearly by varying the number of intervals N, Tab. 1. An equidistant and a non-equidistant mesh are used. The mesh density for the non-equidistant mesh is identical to that used for Fig. 3. We remark that ζ decreases with increasing number of intervals. We can, however, not yet discern a simple convergence low in the numbers of Tab. 1. The reason for this will be found in the complexity of the solution. Important insight is obtained already in the next section.

4.2 Propagation in weakly inhomogeneous plasma

4.2.1 Local dispersion relation

Good insight into the physics and also into the numerics can be obtained from the local dispersion relation. Under the assumption that the plasma is locally homogeneous, it is meaningful to search solutions of eq. (1) of the form $\exp(ik_x x)$. Upon replacing $\partial/\partial x$ by ik_x in eq. (1), one finds

$$a k_x^4 + b k_x^2 + c = 0 \tag{50}$$

where

$$a = \alpha_1 (\alpha_2 - 1) + \alpha_3^2 ,$$

$$b = \alpha_1 C_{00}^{22} + (\alpha_2 - 1) C_{00}^{11} + 2\alpha_3 C_{00}^{12} - k_y^2 , \qquad (51)$$

$$c = C_{00}^{11} C_{00}^{22} + (C_{00}^{12})^2 ,$$

the coefficients $C_{\kappa\lambda}^{\mu\nu}$ being defined by eq. (42).

In Figure 4 the solutions for k_x^2 of eq. (50) are shown as a function of x using for a, b and c their local values calculated for the same physical case as Fig. 3. Only the positive solutions of k_x^2 are shown; these correspond to propagating wave solutions. The fast wave is propagating over the entire plasma volume, whereas the slow wave (or ion Bernstein wave) has merely small propagation regions to the left of the two second harmonic cyclotron resonances where $\omega = 2\omega_{c\ell}$ (ℓ = ^{3}He and D). A physically meaningful solution can be guaranteed only in a part of these latter propagatory regions, namely where $k_x \rho_\ell < 1$.

An excellent test of the code consists in measuring the wavelengths $\lambda = 2\pi/k_x$ in the numerical solution and comparing them with those obtained from the dispersion relation. We have measured all the half periods (maximum-minimum) in the numerical solution for E_x and E_y. The component E_y contains merely long fast-wave wavelengths in the propagation regions of the slow wave. In Figure 4 we have plotted the value of k_x^2 of every third half period of E_x. In the propagatory regions of the slow wave we have added the values of k_x^2 of every half period of E_y. We remark that the agreement is excellent with the exception of the region around -95 cm.

The scattering of the values of k_x^2 in the region around -95 cm is due to insufficient resolution. The shortest wavelength λ that can be represented on a given mesh with mesh size Δx is $\lambda = 2\Delta x$, hence $k_x = \pi/\Delta x$ is the largest possible value of the wavenumber. In the case of the non-equidistant mesh used for Figs. 3 and 4 this largest possible value is a function of x. It is also shown in Fig. 4. The measured wavelengths which are smaller than 2 Δx (see at x = -95 cm) have their origin in oscillations of the cubic functions, eq. (44), between two mesh points.

The solution documented by Figs. 3 and 4 can be made physically more acceptable by increasing ν, the phenomenical damping coefficient. The slow wave will then extend not as far away from the resonances $\omega = 2\,\omega_{c\ell}$ as in Figs. 3 and 4 but will be confined to the regions where $k_x\rho_\ell < 1$. At the same time the mesh will provide sufficient resolution as can be seen in Fig. 4.

4.2.2 WKB-approximation

In Figure 4 one notes that the wavelength of the fast wave does not vary too rapidly across the plasma column or, more precisely, $(1/k_x)d\ell nk_x/dx \ll 1$. This inequality is one of the prerequisites for the application of the WKB-method. Physical situations as the one in Fig. 4 are indeed being extensively studied by the RF-community [20] using the WKB-method in what is known as ray-tracing codes.

Here, we mention the WKB-method for two reasons. First, it provides us with still another good test for our numerical solution:

Far away from the resonances at x = 0 and x = -75 cm our solution should have the WKB-behaviour. Second, by introducing the WKB-solution we make the numerical results accessible for all those people who study propagation and mode conversion by means of asymptotic analysis [21].

We are interested in a WKB-description of the fast wave only. The differential equation describing the fast wave alone is obtained from eq. (1) by dropping the terms proportional to the square of the ion Larmor radii ρ_1, viz. $\vec{\alpha}_x = \vec{\alpha}_y = 0$. Dropping the ion Larmor radii is equivalent to using the cold plasma model from the outset. After elimination of E_x one obtains [11]

$$\frac{d}{dx}\, g(x)\, \frac{dE_y}{dx} + h(x)\, E_y = 0, \tag{52}$$

where

$$\left.\begin{aligned} g(x) &= (\varepsilon_\perp - k_z^2)/\varepsilon_F, \\ h(x) &= \varepsilon_\perp - k_z^2 + \varepsilon_{xy}^2/\varepsilon_F - \frac{d}{dx}\left(ik_y \varepsilon_{xy}/\varepsilon_F\right), \\ \varepsilon_F &= \varepsilon_\perp - k_y^2 - k_z^2 . \end{aligned}\right\} \tag{53}$$

The general WKB-solution of eq. (52) has the form [21]

$$E_y = I_+ + I_-, \quad I_\pm = C_\pm \exp\left[\pm i \int^x k_F\, dx\right] / (g k_F)^{1/2} \tag{54}$$

where

$$k_F = (h/g)^{1/2} \tag{55}$$

and C_+ and C_- are arbitrary complex constants describing the amplitudes of the waves propagating to the right and to the left respectively. Note that for the WKB-method it is necessary to assume that g(x) and h(x) are real. In our context, this implies that the phenomenological damping ν should vanish in the regions where WKB is applied. The damping ν, however, affects above all the slow wave. For this reason we shall further analyse the numerical results already obtained (Fig. 3 and 4) and not even bother to set ν to zero. We simply take for g and h the real parts of their definition in eq. (53).

From the values of E_y and E_y' at a given spatial point we can compute I_+ and I_-,

$$I_\pm = \left[ik_F \mp \frac{d}{dx}(gk_F)^{-1/2}\right]E_y \pm E_y' , \qquad (56)$$

and the corresponding Poynting fluxes

$$S_\pm = \pm \frac{c^2}{8\pi\omega} k_F |I_\pm|^2 . \qquad (57)$$

If WKB holds S_+ and S_- must be approximately constant and their sum, $S_{tot} = S_+ + S_-$ must be equal to the total energy flux, S_x, eq. (33). The results are shown in Fig. 5. The quantities S_+, S_-, S_{tot} and S_x have been computed by means of the numerical solution for E_x, E_x', E_y and E_y'. Every fifth spatial point only is used for Fig. 5.

First, we remark that all the traces are quite smooth in the regions $-70 \leq x \leq -10$ cm and $10 \leq x \leq 120$ cm. It is in these regions that the WKB method should be applicable. Furthermore we remark that S_x and S_- are not completely flat in these regions. This is imputable to the influence of the damping ν: the fast wave is slightly damped. In spite of the damping the relation $S_{tot} \approx S_x$ holds everywhere except in the regions where the slow wave exists (compare Figs. 3 and 4). In the neighbourhood of these regions and also near the left boundary, the WKB-approximation does not or only barely hold. We conclude that the numerical solution exhibits the WKB-behaviour there where it should.

4.3 Eigenmodes of the fast magnetosonic wave

In situations with weak damping or weak conversion, it may happen that the antenna loading resistance, eq. (25), exhibits distinct peaks when certain parameters like the exciting frequency or the plasma density are varied [9,11]. These peaks can usually be explained by the excitation of eigenmodes of the plasma column [9,11,23]. Both the slow wave and the fast wave can possess eigenmodes. So far only the eigenmodes of the fast wave have been invoked to explain certain phenomena in the ion-cyclotron range of frequency.

Here, we discuss the eigenmodes of the fast wave in a very simple model plasma; we assume homogeneous density, magnetic field and negligible temperatures. In this case, and after certain additional simplifying assumptions, it is possible to determine the eigenmodes and

eigenfrequencies analytically. The purpose of this calculation is again twofold: While demonstrating a fundamental piece of physics we check the computer code.

We solve eqs. (5) and (52) using the boundary condition, eq. (7), and the matching conditions eqs. (11) and (14) for a cold plasma, i.e. $\alpha_i \equiv 0$. There is no driving force (antenna) in the vacuum. On the whole there are six conditions for six unknowns. The unknowns are the coefficients C_1 and C_2 of the solutions in the vacuum regions, eq. (6), and in the plasma,

$$E_y = C_1 e^{ik_F x} + C_2 e^{-ik_F x} \tag{58}$$

The resulting dispersion relation has the form

$$(X+iY)/(X-iY) = \exp(4ik_F x_p) \tag{59}$$

where

$$\left.\begin{aligned} X &= \left\{ k_F^2 (\varepsilon_\perp - k_z^2)^2 - k_y^2 \varepsilon_{xy}^2 - F^2 \varepsilon_F^2 \right\} / \varepsilon_F^2 , \\ Y &= 2 F k_F (\varepsilon_\perp - k_z^2) / \varepsilon_F , \\ F &= (k_z^2/\kappa) \coth[\kappa (x_s - x_p)] . \end{aligned}\right\} \tag{60}$$

Here we have used $x_p \equiv -x_{pl} = x_{pr}$ and $x_s \equiv -x_{sl} = x_{sr}$. Remember that $\kappa^2 = k_y^2 + k_z^2$. The dispersion relation, eq. (59),

could be solved numerically. For our purpose, however, an analytical solution is preferable. To this end, we further simplify our problem choosing a one-species cold plasma such that $\varepsilon_\perp = (\omega^2/v_A{}^2)/(1-\omega^2/\omega_{ci}{}^2)$ and $\varepsilon_{xy} = i(\omega^2/v_A{}^2)(\omega/\omega_{ci})/(1-\omega^2/\omega_{ci}{}^2)$ where v_A denotes the Alfvén velocity. Here we consider the limit $x_p k_z \ll 1$.

As in cylinder geometry [23] the lowest frequency solutions (the so-called surface modes) are obtained under the assumption that $k_F^2 < 0$ and $\omega \sim k_z v_A$. As there are two surfaces in the present case, two eigenfrequencies are found. For $\omega \ll \omega_{ci}$, one finds

$$\omega_{1,2} = k_z v_A \left\{ 1 + \Omega_{1,2}(k_y x_p) \coth\left[k_y (x_s - x_p)\right] \right\}^{1/2}, \qquad (61)$$

where $\Omega_1(r) = \tanh(r)$ and $\Omega_2(r) = \coth(r)$.

The usual eigenmodes of the fast wave are obtained from eq. (59) assuming that $k_F^2 > 0$. From $\tan 2k_F x_p = Y/X \sim x_p{}^2 k_z{}^2 \ll 1$ one concludes that

$$\omega_\ell = v_A \left[k_y^2 + (\ell-2)^2 \pi^2/(2x_p)^2 \right]^{1/2}, \quad \ell = 3, 4, \ldots . \qquad (62)$$

The analytical results, eqs. (61) and (62), can be compared with the frequencies at which one finds a resonant response on P/A, eq. (25), in the numerical solution. The code is run with 10 equi-

distant intervals and the following physical parameters: hydrogen plasma, density $6.38 \cdot 10^{12}$ cm^{-3}, $B_0 = 4.5$T, ion temperature 650 eV, geometrical dimensions $x_p = 18$ cm, $x_a = 21{,}6$ cm, $x_s = 27$ cm, antenna structure $k_y = 5.56 \cdot 10^{-2}$ cm^{-2} and $k_z = 2.78 \cdot 10^{-3}$ cm^{-1}. The phenomenological damping is $\nu = 3 \cdot 10^{-4}$. The results are shown in Tab. 2 for the linear frequencies $f = \omega/2\pi$. Good agreement is found between the analytical and the numerical results. The remaining slight discrepancy at low frequency is due to the approximation $x_p k_z \ll 1$ and the influence of the damping ν.

The quality of the numerical method can also be judged from the eigenfunctions. In Figure 6 we compare the numerical eigenfunction associated with ω_5 with the analytical solution,

$$E_y^{(\ell)} = C \sin\left[(\ell-2)\frac{\pi}{2}\frac{x}{x_p} + \frac{\ell}{2}\pi + \chi\right], \quad \ell = 3, 4, \ldots,$$

$$tg\,\chi = (\omega_{ci}/v_A k_y)\left\{1 + \left[\frac{2 k_y x_p}{(\ell-2)\pi}\right]^2\right\}^{-1/2}. \qquad (63)$$

The free constant C has been chosen to be $-1.216 \cdot 10^{-11}$i in order to fit the numerical results. The numerical solution differs from the analytical one by less than the line width. If we drew the piecewise cubic polynomial, eq. (44), it would be impossible to distinguish it from the analytical solution. As few as four intervals should be enough to obtain a reasonable solution for the function shown in Fig. 6.

Before turning to the phenomenon of linear mode conversion let

us make one remark concerning the graphical representation of numerical solutions. We never show the piecewise cubic polynomials but polygons connecting the functional values at the grid points. In the case of a discretisation with cubic Hermites, the numerical solution, therefore, is always smoother than its graphical representation. As an example imagine the polygon connecting the 11 dots in Fig. 6.

4.4 Linear mode conversion

If we have to treat linear mode conversion analytically as it was necessary before the advent of the computers [24,25], we would now embark upon the presentation of highly sophisticated methods [26,27] which, at the end, would allow us to solve eq. (1) in a few limited cases. A sufficient physical understanding of linear mode conversion can, however, be achieved by studying a basic tutorial text such as Refs. [28,11] and a short numerical illustration as we shall present in the remainder of the present chapter and in Ch. 6.

For the purpose of the numerical illustration, it is sufficient to remark that the slow and the fast waves interact merely in spatial regions where their wavelengths are comparable (confluence). Figure 4 can serve as an example. The wavenumber of the slow wave tends towards the one of the fast wave at x = 0 cm and x = -75 cm. It is at these points that the slow wave is excited by the fast wave.

Under the physically meaningful assumption that $|a| \ll |b^2/c|$ the dispersion relation ,eq. (50), has two obvious approximate solutions,

viz. $k_x^2 = k_F^2 \equiv -c/b$ and $k_x^2 = k_S^2 \equiv -b/a$ corresponding to the fast and the slow waves, respectively. In general, the slow wave has a much shorter wavelength than the fast wave, $|k_S^2| \gg |k_F^2|$; there are, however, two situations where $k_S^2 \approx k_F^2$, the first one being a <u>cutoff</u> of the slow wave, i.e. a region where $k_S^2 \to 0$ as in Fig. 4, and the second one being a <u>resonance</u> of the fast wave, i.e. a region where $k_F^2 \to \infty$. Subsequently, we shall discuss these two cases separately.

Before doing so we release, however, eq. (1) from all its detailed physical ballast, eqs. (2), (3) and (4), in order to make the problem more accessible for mathematically-minded people who like to deal with simple model equations. We assume that $\alpha_2 = \alpha_3 = 0$; $a = -\alpha_1 \neq 0$ is sufficient for the existence of the slow wave. From eqs. (42) and (51) one then concludes that $b \approx -\varepsilon_\perp + k_z^2$ and $c = \varepsilon_F(\varepsilon_\perp - k_z^2) + \varepsilon_{xy}^2$ to lowest order in $|a| \ll 1$. Apart from the geometrical and the antenna parameters only $\varepsilon_\perp$, ε_{xy} and $\alpha_1 = \alpha + i\nu$ are left as free parameters. For the purpose of our illustration only one out of three will depend on x, the others being constant. The case of the resonance we treat with $\varepsilon_\perp = \Xi(x)$ and the cutoff with $\alpha = 1/\Xi(x)$, respectively. The function $\Xi(x)$ is a smooth step function determined by three real parameters Ξ_0, d and ξ_0:

$$\Xi(x) = \Xi_0 (x + i\xi_0) / (d^2 + |x + i\xi_0|^2)^{1/2}. \qquad (64)$$

4.4.1 Cutoff of the slow wave

In Figure 7 a typical wave form is shown for the case where the slow wave has a cutoff. The geometrical and antenna parameters used are similar to the ones of Fig. 3: $x_{pr} = |x_{pl}| = 125$ cm, $x_a = 150$ cm, $x_{sr} = |x_{sl}| = 170$ cm, $k_y = 0.01$ cm^{-1}, $k_z = 0.03$ cm^{-1}, $\omega/2\pi = 55$ MHz. The "plasma" parameters are $\varepsilon_\perp = -0.06$ cm^{-2}, $i\varepsilon_{xy} = 0.13$ cm^{-2}, $\nu = 3 \cdot 10^{-4}$ and $\alpha = 1/\Xi(x)$ where $\Xi_0 = 200$, $d = 25$ cm and $\xi_0 = -0.03$ cm. A non-equidistant mesh with $n = 1500$ intervals has been used. The density of the mesh points is proportional to $1 + 5\exp[-1/2(x/5)^2]$.

With these parameters the fast wave is propagatory throughout the whole plasma. In contrast to Fig. 4 it enters the conversion region from the high magnetic field side. With $\Xi_0 = -200$ we would obtain the corresponding low field side case. Apart from the central region -5 cm $\leq x \leq 5$ cm we have $k_F^2 \approx 0.2$ cm^{-2}. The slow wave is propagating for $x \geq 0$ only. Its wavenumber square is $k_S^2 \approx 10$ cm^{-2} for $x \geq 30$ cm and is zero in the center of the plasma. The slow wave can clearly be seen on the traces of E_x and barely on those of E_y. This is a result of the kinetic and electrostatic nature of the slow wave. It is excited by the fast wave at its cutoff ($k_S^2 = 0$) and propagates from there to the right. Its amplitude diminishes because of the phenomenological damping ν. With a smaller value of ν the slow wave would reach the right boundary. A small-amplitude slow wave is excited directly at the boundary and travels to the left. Here, we are not interested in this effect.

From the WKB-analysis, eq. (57), we can obtain a quantitative picture of how the energy is distributed between the different waves. The incoming energy, $S_- = -1.1 \cdot 10^{-15}$ erg/cm^{2}sec and the reflected energy, $S_+ = 1.3 \cdot 10^{-16}$ erg/cm^{2}sec, respectively. Hence 90% of the total incoming energy is converted into the slow wave and subsequently dissipated. On the left of the conversion region ($x_{pl} \leq x \leq 0$), we have a standing fast wave with $|S_-| \approx S_+ \approx 3 \cdot 10^{-16}$ erg/cm^{2}sec. This situation is different from the situation usually encountered in asymptotic analysis where only a transmitted wave is present on the left side ($S_- \neq 0$ but $S_+ = 0$ at $x \leq 0$).

4.4.2 Resonance of fast wave

In Figure 8 a typical wave form is shown for the case where the fast wave has a resonance. We have used the same parameters as in Fig. 7 with the exception of $x_{pl} = -25$ cm, $\omega/2\pi = 30$ MHz, $k_z = 0.05$ cm^{-1}, $i\varepsilon_{xy} = 0.07$ cm^{-1}, $\alpha = 0.005$, $\varepsilon_\perp = \Xi(x)$ with $\Xi_0 = 0.05$ and $\xi_0 = 0$. In contrast to Fig. 7 an equidistant mesh with 1500 intervals has been used here.

Both the slow and the fast wave are propagatory for $x > 0$ only, corresponding to the physical situation of a fast wave incident from the high field side again (as on Fig. 7). The wavenumber of the fast wave increases from $k_F^2 = 0.044$ cm^{-2} at the right boundary towards a complex value of the order of 1 near the centre (-3 cm $< x \leq 3$ cm). In this region the wavenumber of the slow wave computed from eq. (50) is comparable to the one of the fast wave. The slow wave has in fact a

cutoff where the fast wave has a resonance (x = -1.2 cm) in the simple picture $k_F^2 = -c/b$, $k_S^2 = -b/a$, b = 0. In the region $x \gtrsim 40$ cm, the slow wave is characterised by $k^2 \approx 10\ cm^{-2}$. As in the previous case, Fig. 7, the slow wave is excited in the region of confluence and propagates from there to the right. It is absorbed before reaching the right boundary. From the WKB-analysis we learn that all the energy propagating inwards ($S_- = -9.3 \cdot 10^{-16}$ erg/cm^{2}sec) is converted into the slow wave and absorbed by the phenomenological damping.

The rate of energy conversion does not depend on the properties of the slow wave as long as the slow wave is sufficiently damped, such that it does not reach the boundary and hence does not set up standing waves. One can, in fact, take the limit $\alpha_1 \to 0$ or equivalently $k_S^2 \to \infty$ and finds always the same energy conversion and, clearly, the same wave form for the fast wave. The extreme case, $\alpha_1 = 0$, will be discussed next.

4.5 The cold plasma description

If $\vec{\vec{\alpha}}_x = \vec{\vec{\alpha}}_y = 0$ or, equivalently, if all the temperatures are zero, eq. (1) reduces to the second order equation, eq. (52), the cold plasma model. This equation is singular at points where g(x) = 0 or $\varepsilon_\perp(x) = k_z^2$. The correct interpretation of the singularity provides a description of the mode conversion into the slow wave. The singularity is intimately related to the existence of a continuous spectrum of eigenfrequencies [29] which has extensively been discussed in the connection with Alfvén wave heating [10,11]. The interpretation of this spatial singularity is analogous to the one of the singularity in the

in the velocity space leading to Landau damping. The causality prescribes the way in which the pole has to be treated. The transformation $\omega \to \omega + i\nu$, $\nu > 0$ ensures causality in the case where $\vec{\vec{\varepsilon}}$ is given by the physical expressions ($T = 0$!). In our simplified model equation it is sufficent to have $\xi_0 < 0$ in $\varepsilon_\perp = \Xi(x)$, eq. (64).

The cold plasma model is adequate for the description of the fast wave and the rate of conversion to the slow wave. As a proof in Fig. 9a, we superpose the wave forms as obtained from the cold and the warm models for the parameters used for Fig. 8. We remark that near the boundary the wave form obtained with the cold model is identical to that obtained with the hot model. The antenna loadings differ by 0.7% in the two cases. For the global solution (observed from "outside") it is irrelevant whether the converted energy is dissipated near the resonance as in the cold plasma case or whether it is convected away by the slow wave as in the hot plasma case. The only restriction to this important well-known finding is that the slow wave may not reach the boundary of the plasma. It must be damped before.

As a further illustration in Fig. 9b and 9c, we show two additional cases where the slow wave has a five-times shorter wavelength ($\alpha = 0.001$) and is once weakly ($\nu = 2 \cdot 10^{-5}$) and once heavily damped ($\nu = 3 \cdot 10^{-4}$). In each case, the solution of the cold model (which is identical in Figs. 9a, 9b and 9c) describes the wave field correctly in regions where the slow wave does not exist.

We conclude that in situations where the linear mode conversion is caused by a resonance of the fast wave, the cold plasma description

can be used. Examples are the Alfvén [10] and the ion-ion hybrid resonance [26] and also the resonance of laser light at the local plasma frequency [3, 11]. For certain ICRF minority heating schemes, however, it is essential to use the hot plasma model because the resonance is situated near to cyclotron absorption regions [30].

5. CONVERGENCE PROPERTIES OF THE NUMERICAL SCHEME

The quality and the reliability of a numerical scheme can best be judged from a thorough investigation of its convergence properties. Such an investigation implies numerical analysis and test runs. For space reasons, however, in this paper we present merely partial results concerning the rate of convergence of three quantities. These quantities are the maximum of the absorbed power density, max Q, eq. (32), the absolute value of E_x at the boundary, $|E_x|$, and the real part of the power per area emitted by the antenna, P/A, eq. (25).

The results are obtained and presented in the following way. The case shown in Fig. 8 is used as a test case. Runs are made with as few as 25 and as many as 1800 intervals. Cubic (Fig. 10) and linear elements (Fig. 11) are used. Let the results obtained with N intervals be X_N, standing for max Q, $|E_x|$ or P/A, respectively. From apreliminary graph X_N versus N^{-r} we graphically obtain an approximate converged X_∞. The exponent r must be chosen conveniently. It might be r = 2, 3, 4, 5 or 6. Once X_∞ is obtained, one defines

$$\theta(X) = \left| \frac{X_N - X_\infty}{X_\infty} \right| . \qquad (65)$$

It is this quantity which is depicted in Figs. 10 and 11.

The most striking result in Fig. 10 is the extremely high convergence rate of P/A, $\sim N^{-6}$. Also interesting is the quality of the solution in absolute values: the solution is acceptable to a physicist (say $N \approx 200$) before it settles to its final convergence law at $N \approx 500$.

In contrast to Fig. 10, for linear elements we find in Fig. 11 a low convergence rate for max Q. The rate is in fact so low that we need almost 2000 intervals in order to obtain an acceptable precision of the order of 1%. We conclude therefore that linear elements behave reasonably but that the precision is by far much lower than that achieved with cubic elements.

6. AN APPLICATION: THE BUDDEN EQUATION AND ITS NATURAL EXTENSION

The method described here has already been applied to a number of different physical situations, mainly for JET [1,30,31]. Here we present an application to a model equation which, together with its extensions, is often used by the ICRF community [9,25,26]: the Budden equation. The equation in its primitive form reads

$$\frac{d^2E_y}{dx^2} + k_0^2\left(1 - \frac{\tau}{x}\right)E_y = 0 \qquad (66)$$

and can be obtained from the equation for the cold plasma, eq. (52), by setting $k_y = 0$, $\varepsilon_\perp = (k_0^2/4\tau)x + k_z^2$ and $\varepsilon_{xy} = i\,(k_0^2/4\tau)\,(x - 2\tau)$.

Causality can be ensured by adding $i\nu$ to ε . Here, however, we shall not use eq. (52) but rather the system of two second order differential equations which is obtained from eq. (1) with ε and ε_{xy} of the form as just mentioned , $\alpha_2 = \alpha_3 = 0$ and $\alpha_1 = \alpha + i\nu$. The equation so-obtained is considered to be the natural extension of the Budden equation.

Equation (66) is a model equation for the mode conversion due to a resonance of the fast wave (see Sect. 4.4.2). The fast wave has a resonance at $x = 0$ and a cutoff at $x = \tau$. Far away from the conversion region its wavelength is given by $2\pi/k_0$. It is possible to determine analytically the transmission, reflection and absorption coefficients T^2, R^2 and A of a fast wave impinging on the conversion region. One can distinguish two main cases depending on whether the wave encounters first the cutoff ($\tau > 0$, LFS) or the resonance ($\tau < 0$, HFS). In the context of the ion-ion-hybrid resonance in ICRF tokamak heating, these two cases correspond to a fast wave excited on the low (LFS) or on the high (HFS) magnetic field side of the torus respectively. The well-known results are

$$\left.\begin{aligned} &\text{HFS}: \quad R^2 = 0\,, \quad T^2 = e^{-\pi/|\tau k_0|}\,, \\ &\text{LFS}: \quad R^2 = \left(1 - e^{-\pi/|\tau k_0|}\right)^2, \quad T^2 = e^{-\pi/|\tau k_0|}\,, \end{aligned}\right\} \tag{67}$$

and $A = 1 - R^2 - T^2$.

Numerically, these coefficients can be determined with the help of the WKB-analysis, presented in Sect. 4.2.2. In the Budden problem it

is assumed that the fast wave is incident from infinity and that the reflected and transmitted waves propagate away to infinity again (asymptotic method). Here, we can set up strong local damping at the plasma edge in order to prevent reflection from the plasma boundary. The wave is then excited by the antenna, is strongly damped in the boundary layer but subsequently propagates freely towards $x = 0$ where it undergoes the conversion process. Of the resulting waves the slow wave is damped as it propagates away from the conversion region (as in Fig. 8) whereas the reflected and the transmitted fast waves travel more or less unaffected to the boundary layer where they are damped. For sufficiently small α (i.e. sufficiently small temperature) there is a region in space between the conversion layer and the damping-providing boundary layer where the energy transport can be described by the Poynting flux associated with the fast wave, eq. (57). Let S_I, S_R and S_T be the Poynting fluxes associated with the incident, reflected and transmitted fast waves. Then $R^2 = |S_R/S_I|$ and $T^2 = |S_T/S_I|$.

A first result is presented in Fig. 12. The point in question here is the approach to the Budden result, eq. (67), as $\alpha > 0$ tends towards zero. The case $\alpha < 0$ is not treated here. The computations have been performed with the following parameters: $x_{pr} = -x_{pl} = 200$ cm, $x_a = 220$ cm, $-x_{sl} = x_{sr} = 1010$ cm, $k_o = 0.2$ cm^{-1} and $\tau = 1$ cm. The non-equidistant mesh consisted of 1500 intervals distributed according to the density $1 + 8 \exp[-1/2(x/40)^2]$. The damping ν had the form

$$\nu = \nu_0 + 3.1\left[e^{-\frac{1}{2}\left(\frac{x-x_{sl}}{20}\right)^2} + e^{-\frac{1}{2}\left(\frac{x-x_{sr}}{20}\right)^2} \right] \qquad (68)$$

and $\nu_o = \alpha/20$. One remarks in Fig. 12 that the deviation from the Budden result is an approximately linear function of the temperature parameter α. For the present parameters, i.e. $4\pi\alpha k_o|\tau| < 0.4$, this finding is not inconsistent with analytical work concerning a simplified forth order differential equation [26,32] for which one finds that $\pi|\tau k_o|$ in eq. (67) has to be replaced by $\pi|\tau k_o(1 + 4\alpha)|$. The tendency in Fig. 12 is correctly described by the $(1 + 4\alpha)$ correction of eq. (67) but the deviation is somewhat larger in Fig. 12.

An overall impression of the effect of the temperature on the mode conversion process can be obtained from Fig. 13. Again, a picture not inconsistent with the analytical work is obtained. Our absorption coefficients are in general, however, larger than those of the analytical model. The peak value, e.g., for the low field side case is 50% higher than the one obtained analytically from eq. (67) using the $(1 + 4\alpha)$ correction.

The established discrepancies are easily acceptable in the view of the fact that both models are highly idealized models for a real rf-heating set-up. They can be used to study the fundamental phenomena of wave conversion and absorption but the ultimate question interesting the physicist, viz. the one concerning the antenna-plasma coupling, is better approached by directly calculating the power emitted by the antenna, eqs. (25) and (26).

In order to evidence the profound difference between an asymptotic analysis, as in eq. (67) and in Figs. 12 and 13, and a full wave solution of the type shown in Figs. 7 and 8 we repeat the calculations

done for $\alpha = 0.02$ in Fig. 13 with $\nu = \nu_o$ instead of eq. (68). The fast wave can now be reflected from the plasma edge and partially standing waves are set up.

In Figure 14 we show the real part of the power per area emitted by the antenna as a function of the "Budden parameter" $k_o\tau$ for two different plasma cavities. The first is identical to the one used for Figs. 12 and 13, the second is half a wavelength longer: $x_{pr} = -x_{pl} = 207$ cm. Most strikingly the traces for the two cavities are entirely different and only the HFS traces have a distant resemblance with those of Fig. 13. The essential physical phenomenon here is the existence of standing waves or global modes (remnants of eigenmodes [23]) which fill the whole or a part of the plasma cavity. Clearly in the case of the LFS excitation, the plasma responds with a resonance in P/A when a global mode is excited. Astonishingly a hole in P/A appears at the same place in the HFS traces. Lossless solutions or holes have been predicted from analytical considerations [32].

A great effort will have to be made in the future to achieve a thorough understanding of the interplay between global modes excited by the external antenna and the mode conversion mechanism. This interplay is an essential feature in most of the ICRF heating scenarios. Figure 14 is not meant as an answer to these questions but rather as a starting point to and a motivation for future investigations.

7. CONCLUSIONS

Standard numerical methods have been used to treat the classical problem of linear wave propagation, conversion and absorption. Both the numerical method and the physical phenomenon are well known. The original feature of the paper resides in the fact of the cohabitation of the two.

We have proven that the finite element method can be applied straightforwardly to linear wave conversion problems in contrast to more primitive numerical methods such as Runge-Kutta shooting procedures. We have shown that it is easy to recover known analytical results concerning energy conservation, local dispersion relation, WKB-solutions, eigenmodes and the equivalence of hot and cold plasma models, in particular concerning the Budden equation.

Investigating the convergence properties of the numerical schemes obtained by using linear and cubic finite elements, we have found that it is advantageous to use the cubic elements. The novice in numerics therefore should vehemently subdue the repulsion he might feel from the higher complexity which the cubic elements engender. He should bear in mind that the part where one can get lost, viz. getting from eq. (40) to eq. (46), is common to any system of differential equations, and could, exceptionally, even be requested from the present authors.

In the past we have often met with analytically-minded people who deeply distrust numerical findings. One main goal of the present paper

was, and we hope having succeeded, to prove the relevance and seriousness of a numerical approach. If this point is accepted we can move ahead and investigate important physical problems such as the interplay between the global modes and the linear wave conversion process in ICRF plasma heating or the propagation and conversion in other frequency ranges than ICRF.

Acknowledgement

The work described here was partially supported by the Swiss National Science Foundation.

References:

[1] T. Hellsten, K. Appert, J. Vaclavik and L. Villard, Nucl. Fusion 25 (1985) 99.

[2] D.W. Ross, G.L. Chen and S.M. Mahajan, Phys. Fluids 25 (1982) 652.

[3] T. Speziale and P.J. Catto, Phys. Fluids 20 (1977) 990 and papers cited therein.

[4] D.G. Swanson, Nucl. Fusion 20 (1980) 949.

[5] P.L. Colestock and R.J. Kashuba, Nucl. Fusion 23 (1983) 763.

[6] B. McVey, "ICRF Antenna Coupling Theory for a Cylindrically Stratified Plasma", MIT Report PFC/RR-84-12, July 1984.

[7] A. Fukuyama, S. Nishiyama, K. Itoh and S.-I. Itoh, Nucl. Fusion 23 (1983) 1005.

[8] S.C. Chiu and T.K. Mau, Nucl. Fusion 23 (1983) 1613.

[9] Y. Lapierre, J. Plasma Phys. 29 (1983) 223.

[10] K. Appert, B. Balet, R. Gruber, F. Troyon, T. Tsunematsu and J. Vaclavik, Nucl. Fusion 22 (1982) 903.

[11] K. Appert, J. Vaclavik and L. Villard, "Lecture Notes: An Introduction to the Theory of Alfvén Wave Heating (with a side-glance on ICRF)", Lausanne Report, LRP 238/84, CRPP 1984.

[12] D.G. Swanson, Phys. Fluids 24 (1981) 2035.

[13] D.L. Book, "NRL Plasma Formulary", Naval Research Laboratory, 1978.

[14] A.B. Mikhailovskii, in Reviews of Plasma Physics, edited by M.A. Leontovich, Vol. 3, Consultants Bureau, New York-London, 1967.

[15] M. Brambilla, Plasma Phys. 27 (1985) 1.

References (cont'd)

[16] T. Martin and J. Vaclavik, submitted for publication to Phys. Fluids, Lausanne Report, LRP 259/85, CRPP 1985.

[17] G. Strang and G.J. Fix, "An analysis of the finite element method", Prentice-Hall, Englewood Cliffs, 1973.

[18] P.M. Prenter, "Splines and Variational Methods", John Wiley & Sons, New York, 1975.

[19] M.H. Schultz, "Spline Analysis", Prentice-Hall, Englewood Cliffs, 1973.

[20] M. Brambilla, Comp. Phys. Reports, invited paper presented at this Conference.

[21] N.S. Erokhin and S.S. Moiseev, in "Reviews of Plasma Physics", Vol. 7, p. 181, Ed. M.A. Leontovich, Consultants Bureau, New York-London, 1979.

[22] A. de Chambrier et al., Plasma Phys. 24 (1982) 893.

[23] K. Appert, J. Vaclavik and L. Villard, Phys. Fluids 27 (1984) 432.

[24] V.L. Ginzburg, "The propagation of electromagnetic waves in plasmas", Pergamon, Oxford, 1970.

[25] K.G. Budden, "Radio waves in the ionosphere", Cambridge University Press, 1961.

[26] T.H. Stix and D.G. Swanson, in "Handbook of Plasma Physics", Vol. 1, p. 335, ed. A. Galeev and R.N. Sudan, NHPC, Amsterdam, 1983.

[27] D.J. Gambier and D.G. Swanson, Phys. Fluids 28 (1985) 145.

References (cont'd)

[28] L.A. Artsimowitsch and R.S. Sagdejew, "Plasmaphysik für Physiker", B.G. Teubner, Stuttgart, 1983.

[29] E.M. Barston, Annals Phys. 29 (1964) 282.

[30] K. Appert, T. Hellsten, J. Vaclavik and L. Villard, Proc. 4th Int. Symp. on Heating in Toroidal Plasmas, Roma, 1984, Vol. I, p. 377.

[31] T. Hellsten, K. Appert, J. Vaclavik and L. Villard, Proc. Int. Conf. Plasma Physics, Lausanne, 1984, Contr. Papers, Vol. I, p. 65.

[32] D.W. Faulconer, Phys. Letters 75A (1980) 355.

Figures Captions:

Fig. 1: Configuration of the slab model. The plasma is situated between two vacuum regions (I + II and III) which are delimited by ideally conducting walls. An idealized antenna is situated in one of the vacuum regions.

Fig. 2: Basic functions of linear (σ_j) and cubic Hermite (ψ_j, ϕ_j) finite element methods.

Fig. 3: Energy conservation in a typical physically relevant run. Upper part shows the dissipated power density Q, eq. (32), versus the spatial coordinate x. The lower part shows the error Δ, eq. (48), in energy conservation which is unsatisfactory on the left side of the absorption peaks.

Fig. 4: Local values of the wavenumber squared (k_x^2) from the dispersion relation, eq. (50), for the fast wave (————) and the slow wave (------). Dots represent measured values obtained from the numerical solution for ReE_x(O) and ReE_y (□). Wavenumbers larger than $\pi/\Delta X$ (••••••) cannot be resolved numerically. Wavenumbers larger than $1/\rho_i$ (-•-•-) are physically questionable.

Fig. 5: Energy fluxes versus radial position x. Shown are the full energy flux S_x(Poynting + kinetic) according to eq. (33), and the Poynting fluxes S_+ and S_- obtained from the WKB-analysis. The sum of S_+ and S_- is shown by a number of circles.

Fig. 6: The imaginary part of the electric field component E_y versus the spatial coordinate x for the 5th eigenmode of the fast wave (or the 3rd eigenmode, if the surface modes, eq. (61), are counted separately). Shown are the analytical solution (————————) and the value Im u_2^j and the derivative Im p_2^j (j = 1,..., 11), eq. (44), of the numerical solution (-0-).

Fig. 7: Solution of the simplified wave equation, eq. (1), where the slow wave has a cutoff at the spatial coordinate x = 0 cm. Shown are all the components of the electric field. In contrast to Figs. 3 and 4, the slow wave propagates to the right.

Fig. 8: Solution of the simplified wave equation, eq. (1), where the fast wave has a resonance at the spatial coordinate x ≈ 0 cm. Shown are all the components of the electric field.

Fig. 9: Superpositions of solutions of the cold (▬▬▬▬) and the hot (————————) plasma wave equation, eqs. (52) and (1) respectively. Shown is the real part of E_x versus the spatial coordinate x. The solution of eq. (51) is identical in the three pictures whereas the solutions of eq. (1) have been obtained with α = 0.005 + i0.0003 (a, top), α = 0.001 + i0.00001 (b, middle) and α = 0.001 + i0.0003 (c, bottom).

Fig. 10: Relative deviation $\Theta(X) = \left|(X_N - X_\infty)/X_\infty\right|$ of three important quantities X from their respective converged values X_∞ versus the number of intervals N. The basis functions are cubic Hermites.

Fig. 11: Relative deviation $\Theta(X)$ versus the number of intervals N. The basis functions are piecewise linear hat functions.

Fig. 12: The deviation from the Budden value of the reflection (R^2) and the transmission (T^2) coefficients obtained from the natural extension of the Budden equation versus the temperature parameter α for high (HFS) and low field side (LFS) excitation. The distance τ between cutoff and resonance is roughly one thirtieth of the wavelength $2\pi/k_o$ of the fast wave ($k_o\tau = 0.2$).

Fig. 13: The absorption coefficient obtained from the natural extension of the Budden equation versus the parameter $k_o\tau$ describing the distance between resonance and cutoff. The results for three different values of the temperature parameter α(-----) are shown together with the Budden value (———) corresponding to $\alpha = 0$, for low and high field side excitation.

Fig. 14: Results obtained from full wave solutions of the natural extension of the Budden equation. Shown is the real part of the power per area emitted by an antenna situated in the high (low) field side vacuum region versus the parameter $k_o\tau$. The results for two plasma cavities of different size (400 cm and 414 cm) are shown. With $k_o=0.2$ cm^{-2} the difference in size corresponds to half a wavelength of the fast wave.

Table 1

N	eq.	non-eq.
250	$1.63 \cdot 10^{-1}$	$2.05 \cdot 10^{-1}$
500	$2.64 \cdot 10^{-1}$	$3.11 \cdot 10^{-2}$
1000	$5.9 \cdot 10^{-2}$	$1.00 \cdot 10^{-2}$
1500	$3.21 \cdot 10^{-2}$	$4.17 \cdot 10^{-3}$

Value of the energy balance parameter ζ, eq. (49), for different numbers of intervals N using an equidistant (eq.) and a non-equidistant (non-eq.) mesh.

Table 2

l	f_{an} [MHz]	f_{num} [MHz]
1	2.79	2.72
2	3.36	3.47
3	63.9	64.3
4	113	114
5	165	166

Eigenfrequencies of the five lowest radial eigenmodes of the fast wave including two surface modes (ℓ = 1,2). The values f_{an} are computed from eqs. (61) and (62) whereas f_{num} are the numerically found resonant frequencies.

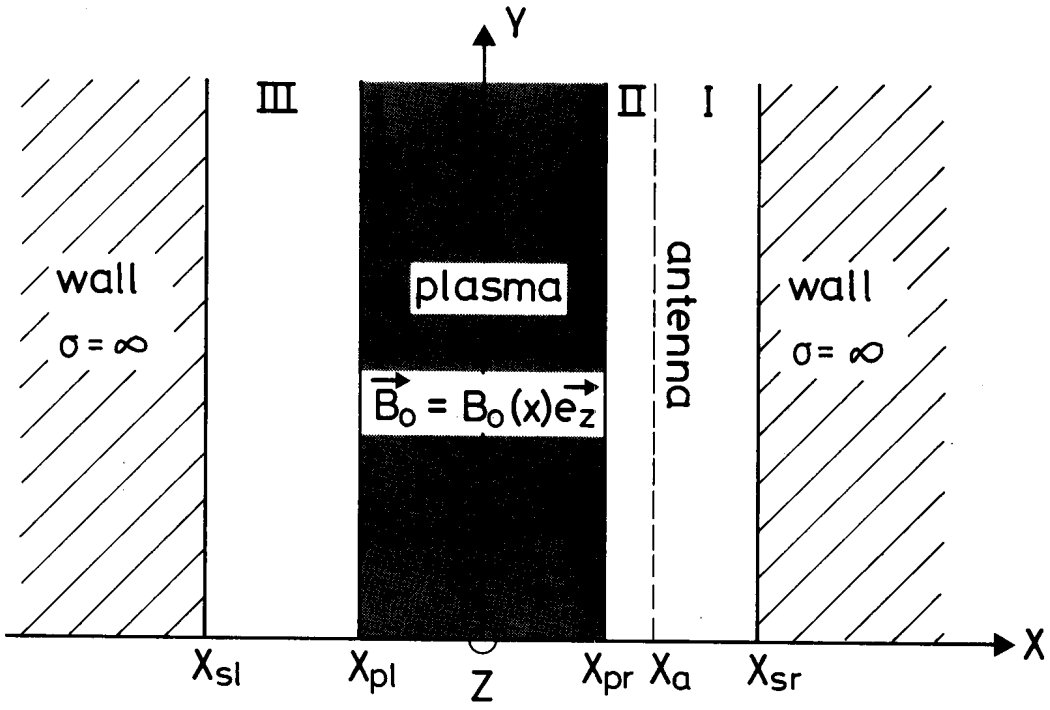
Y
III
II
I
wall
σ = ∞
plasma
$\vec{B_o} = B_o(x)\vec{e_z}$
antenna
wall
σ = ∞
X
X_{sl}
X_{pl}
Z
X_{pr}
X_a
X_{sr}

FIG. 1

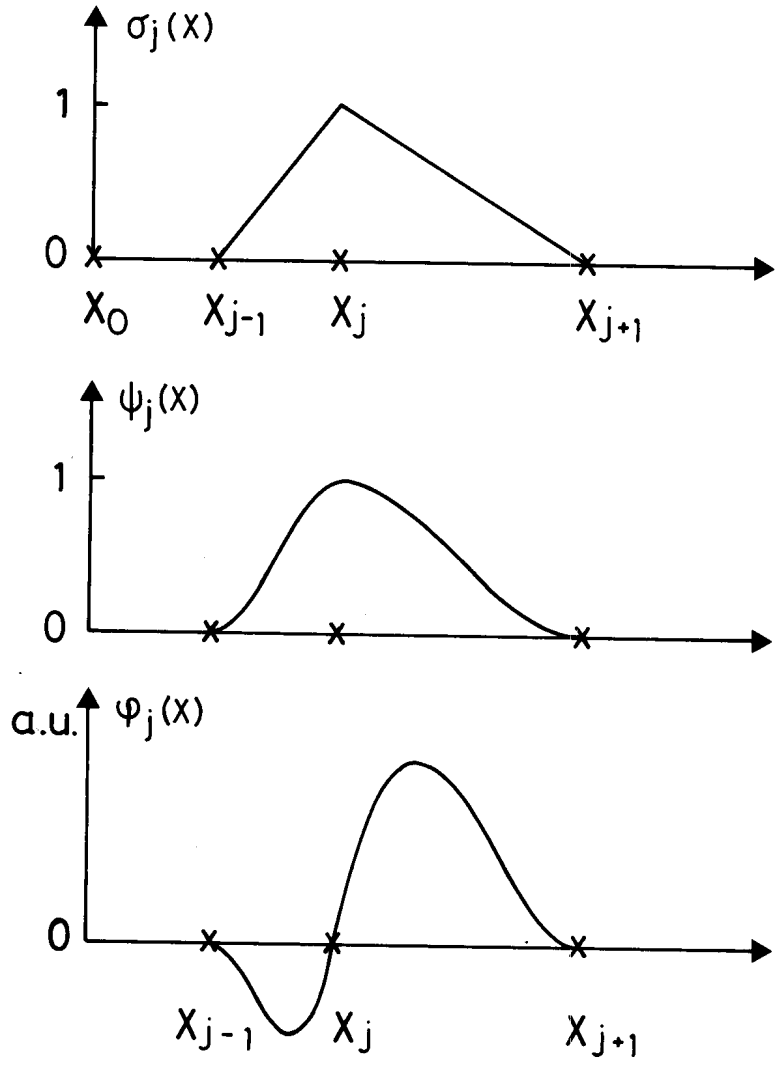

FIG. 2

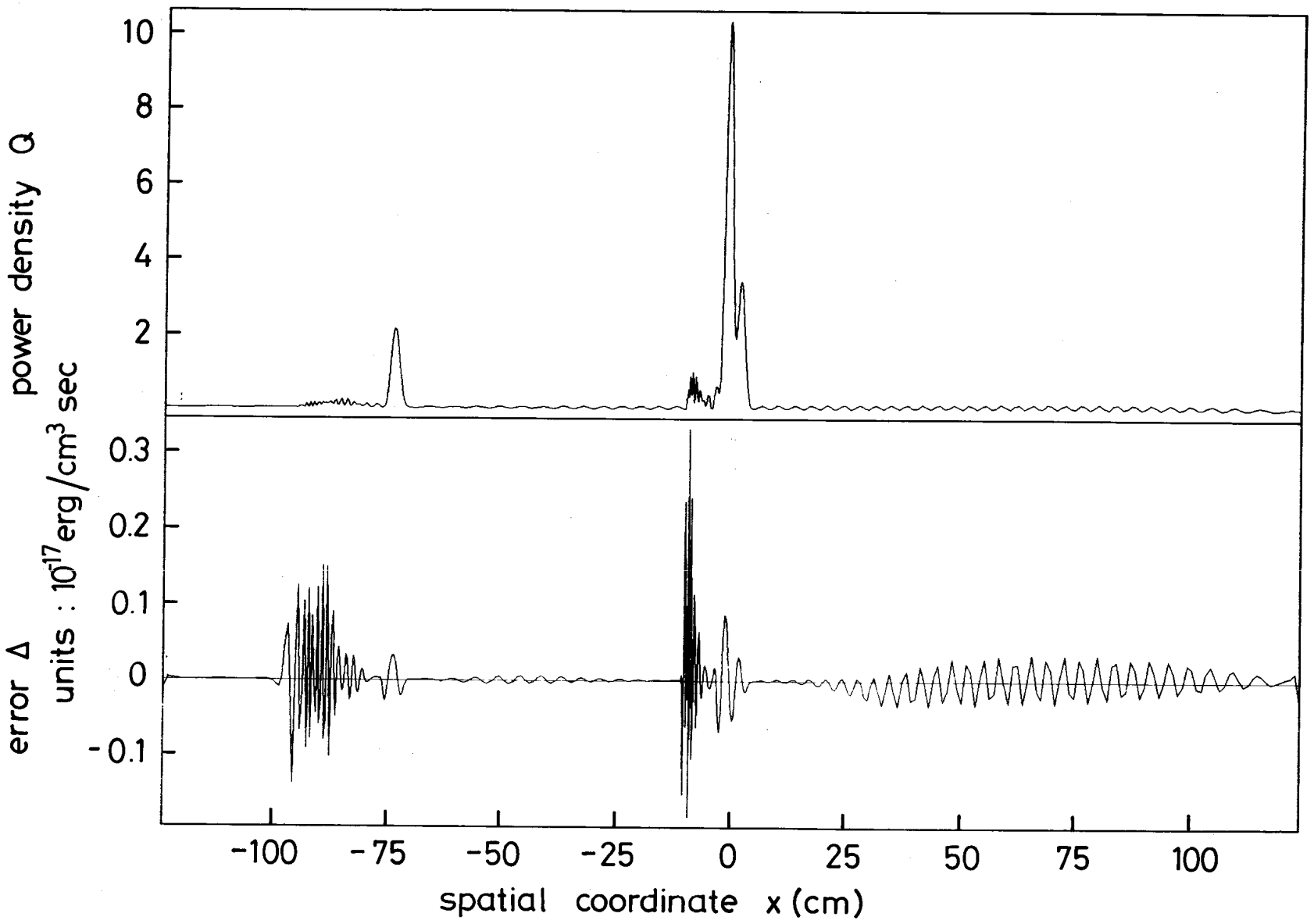
power density Q
10
8
6
4
2
error Δ
units : 10^{-17} erg/cm^3 sec
0.3
0.2
0.1
0
-0.1
-100
-75
-50
-25
0
25
50
75
100
spatial coordinate x (cm)

FIG. 3

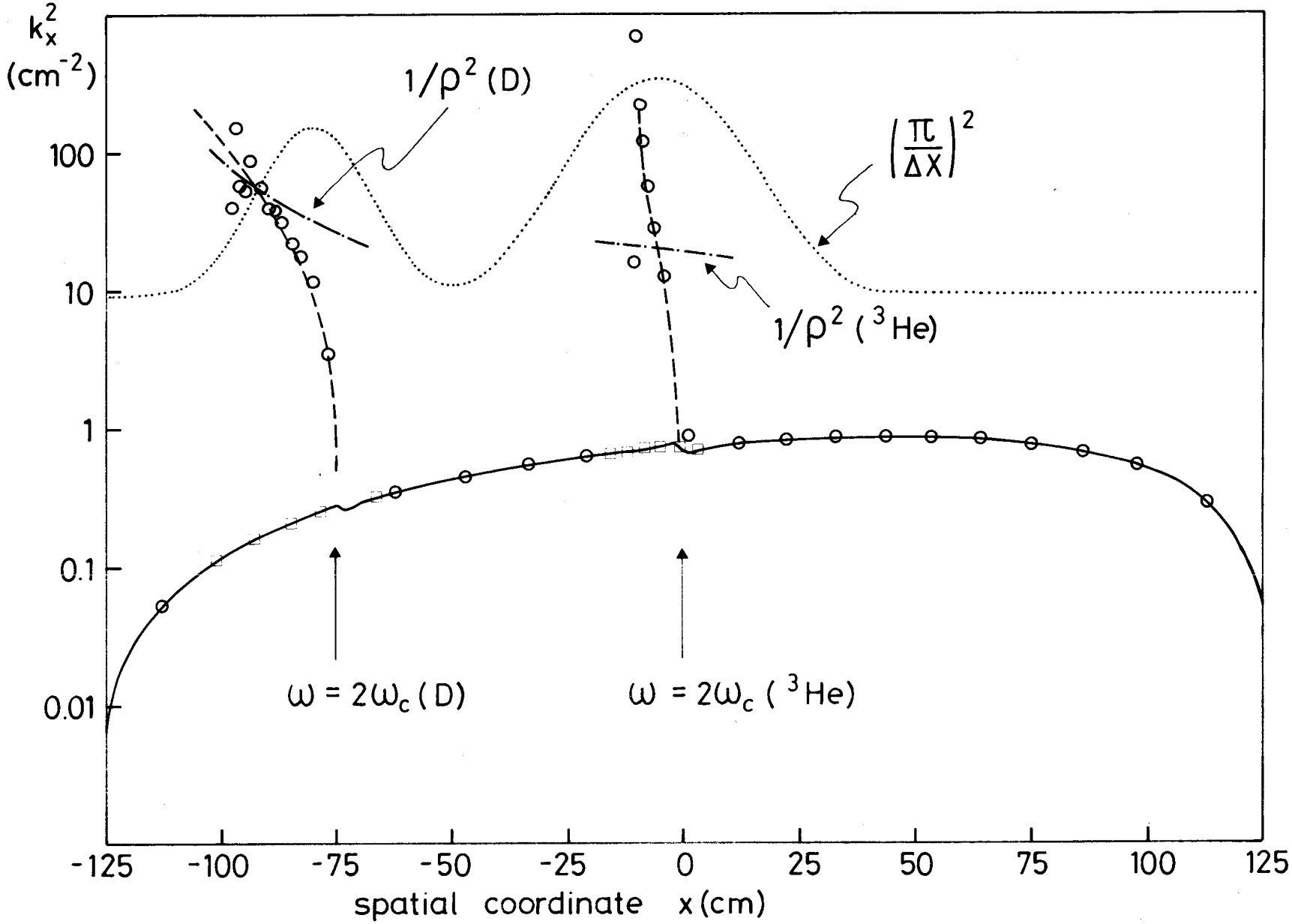
k_x^2
(cm^{-2})
100
10
1
0.1
0.01
$1/\rho^2$ (D)
$\left(\frac{\pi}{\Delta X}\right)^2$
$1/\rho^2$ (^{3}He)
$\omega = 2\omega_c$ (D)
$\omega = 2\omega_c$ (^{3}He)
-125
-100
-75
-50
-25
0
25
50
75
100
125
spatial coordinate x (cm)

FIG. 4

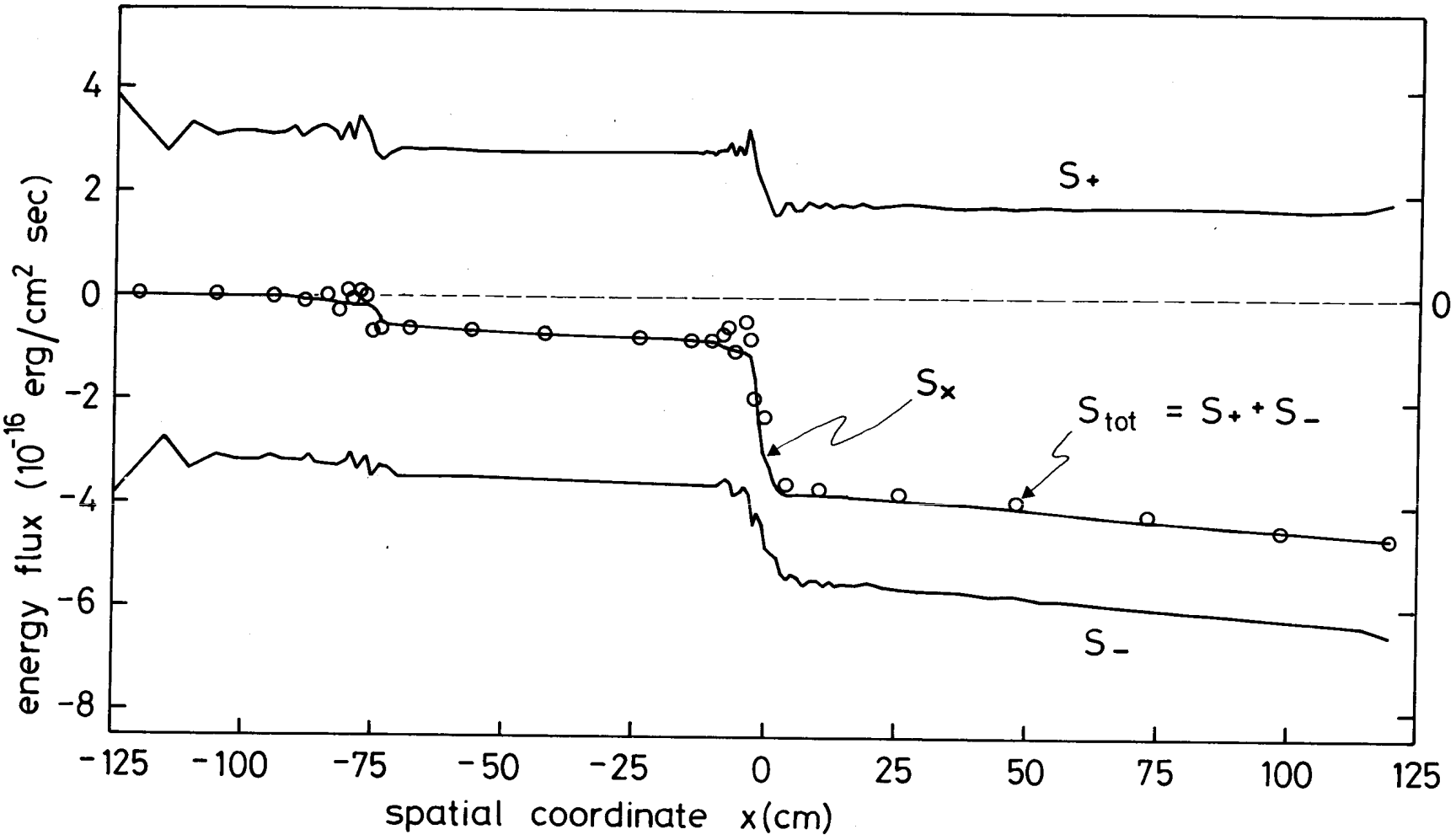
energy flux (10^{-16} erg/cm^2 sec)
4
2
0
-2
-4
-6
-8
S_+
S_x
$S_{tot} = S_+ + S_-$
S_-
0
-125
-100
-75
-50
-25
0
25
50
75
100
125
spatial coordinate x(cm)

FIG. 5

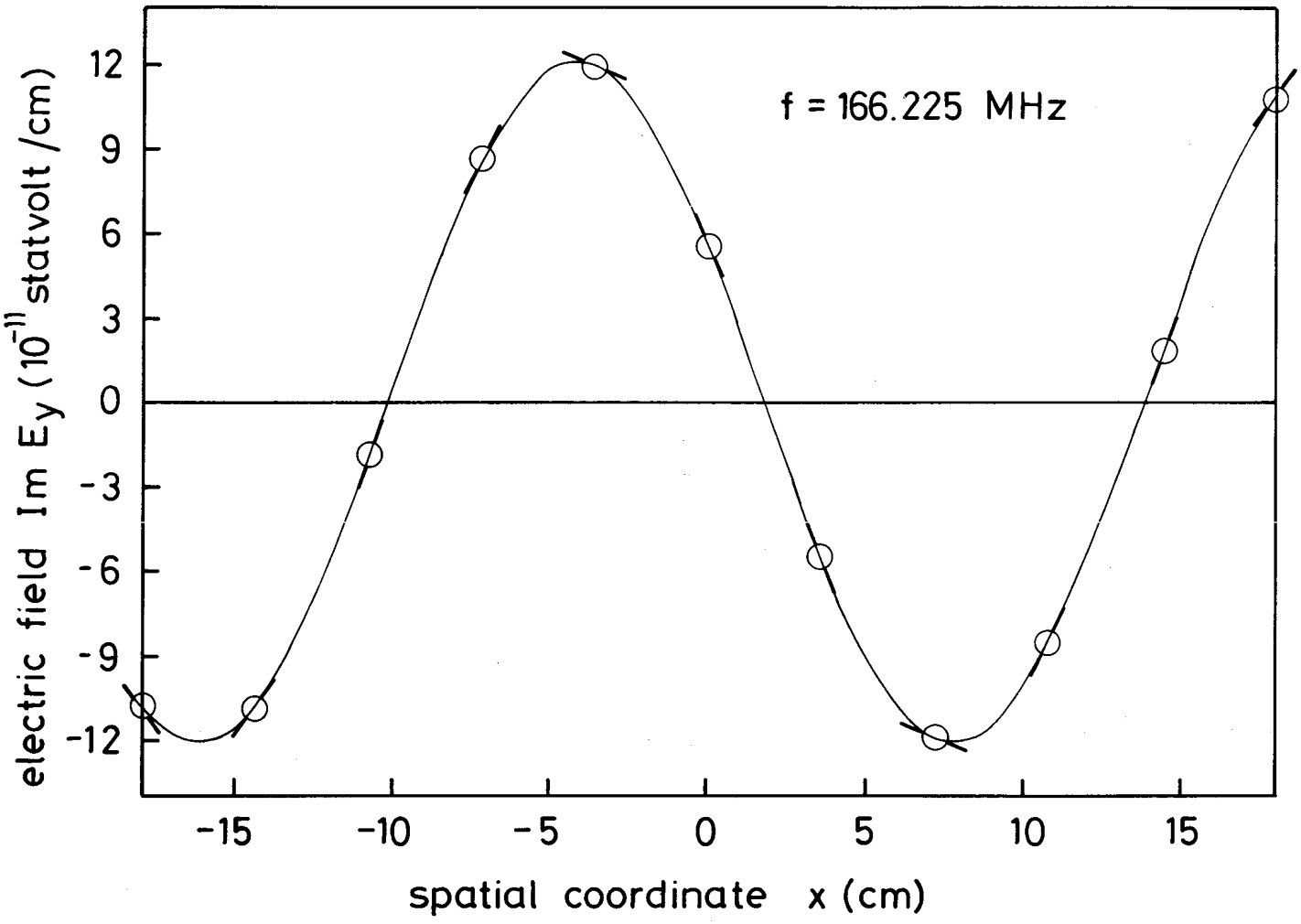
f = 166.225 MHz
electric field Im E_y (10^{-11} statvolt /cm)
12
9
6
3
0
-3
-6
-9
-12
-15
-10
-5
0
5
10
15
spatial coordinate x (cm)

FIG. 6

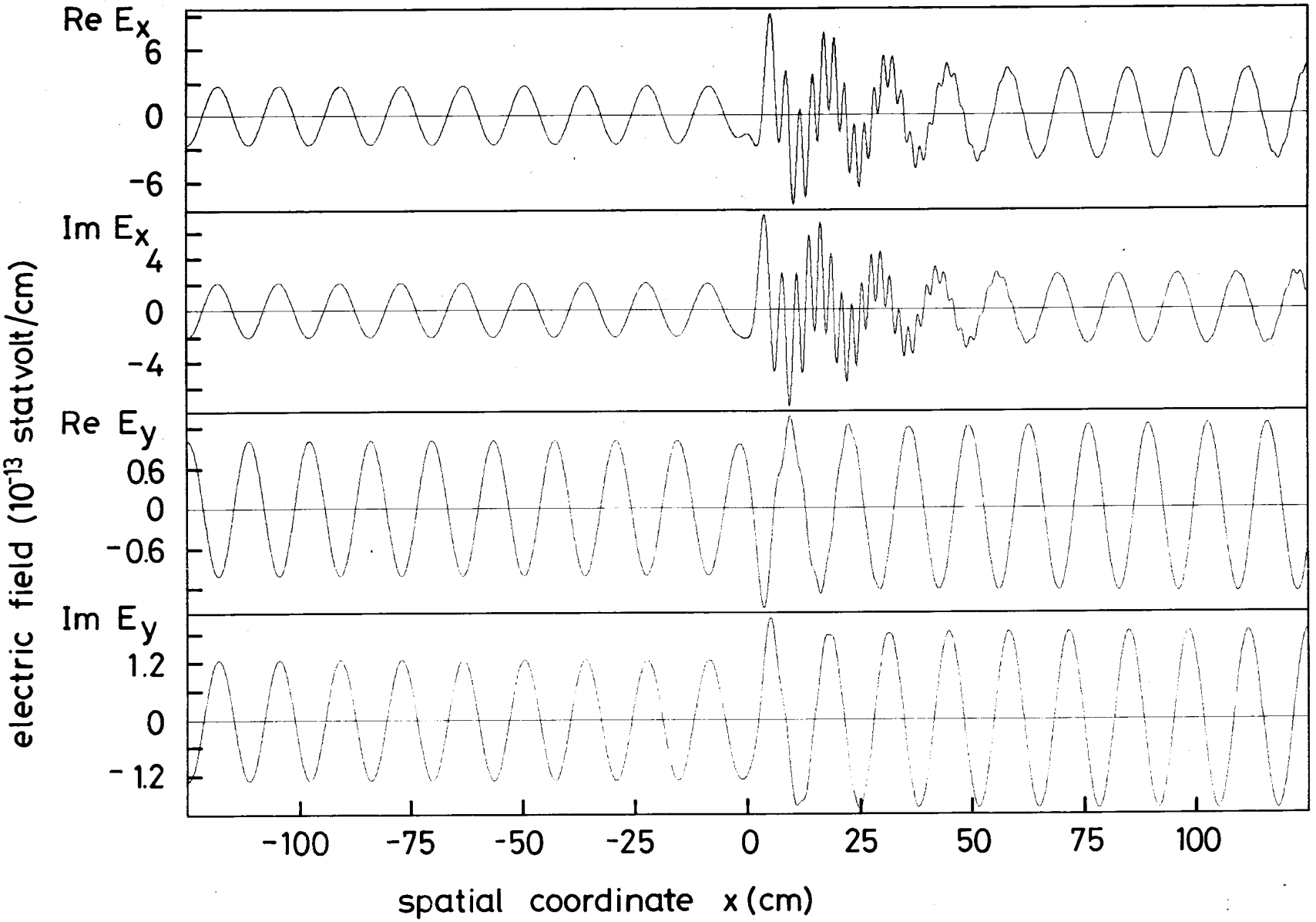
Re E_x
6
0
-6
Im E_x
4
0
-4
Re E_y
0.6
0
-0.6
Im E_y
1.2
0
-1.2
electric field (10^{-13} statvolt/cm)
-100
-75
-50
-25
0
25
50
75
100
spatial coordinate x (cm)

FIG. 7

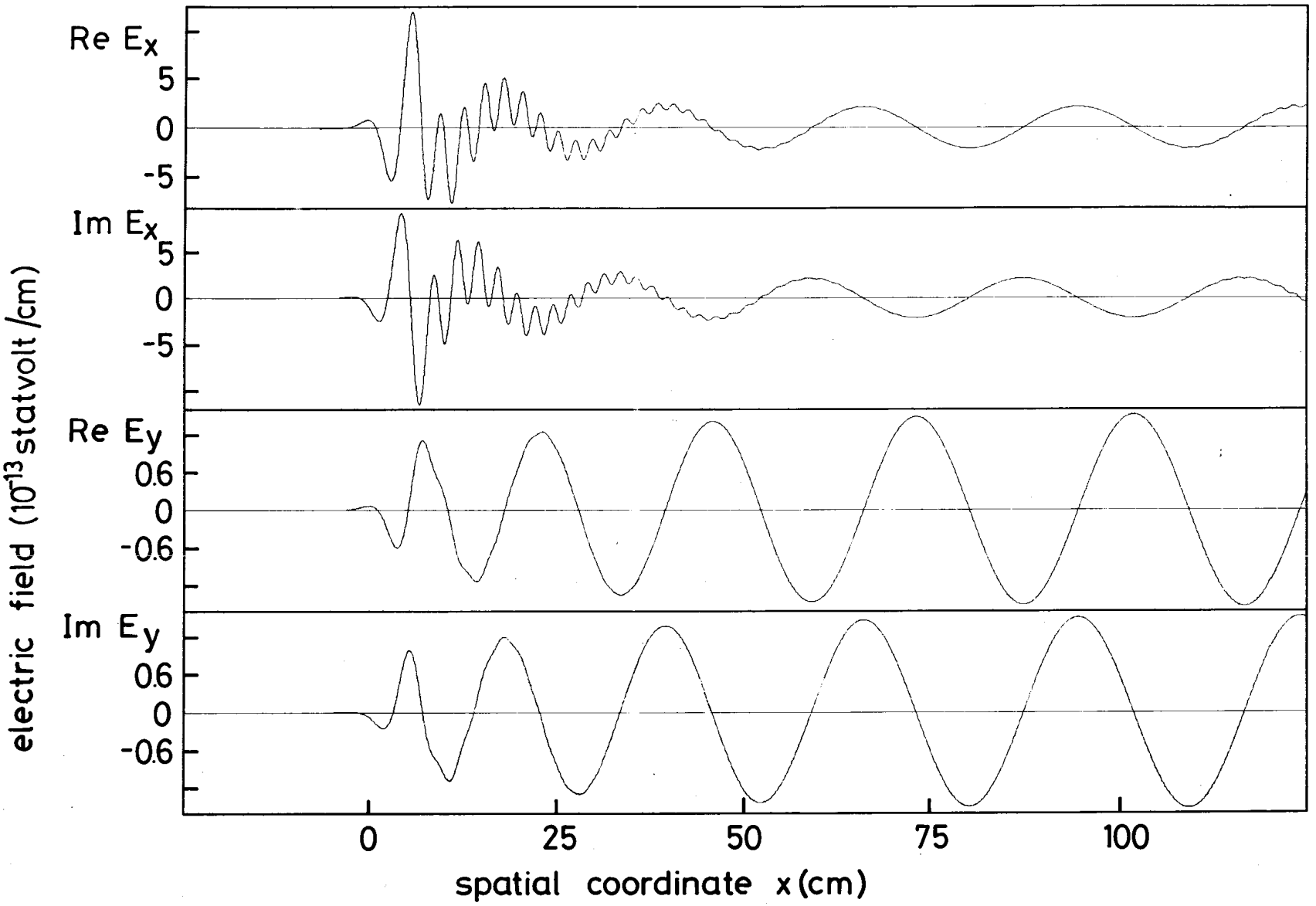
Re E_x
5
0
-5
Im E_x
5
0
-5
Re E_y
0.6
0
-0.6
Im E_y
0.6
0
-0.6
electric field (10^{-13} statvolt/cm)
0
25
50
75
100
spatial coordinate x (cm)

FIG. 8

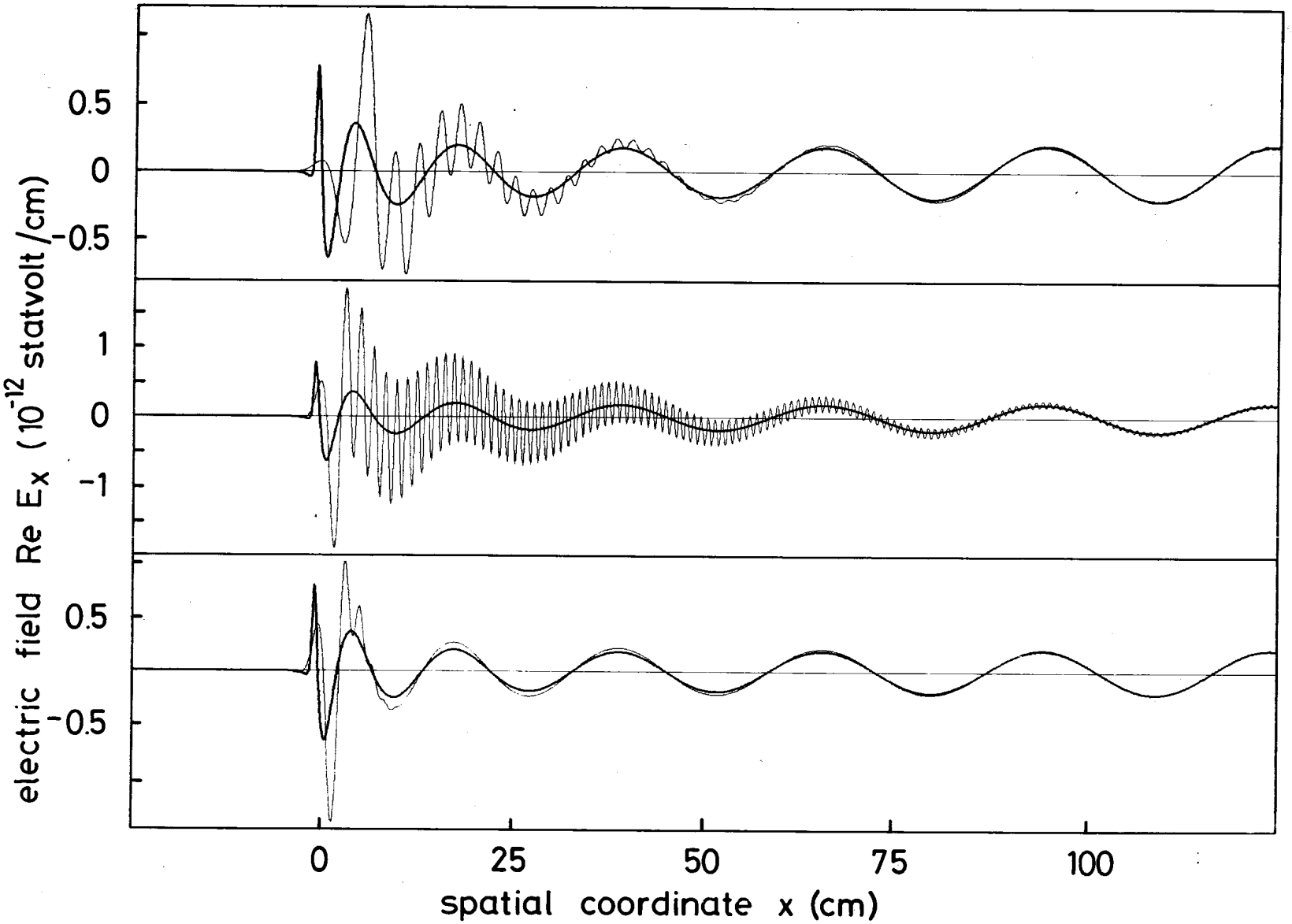
0.5
0
-0.5
1
0
-1
0.5
-0.5
electric field Re E_x (10^{-12} statvolt/cm)
0
25
50
75
100
spatial coordinate x (cm)

FIG. 9

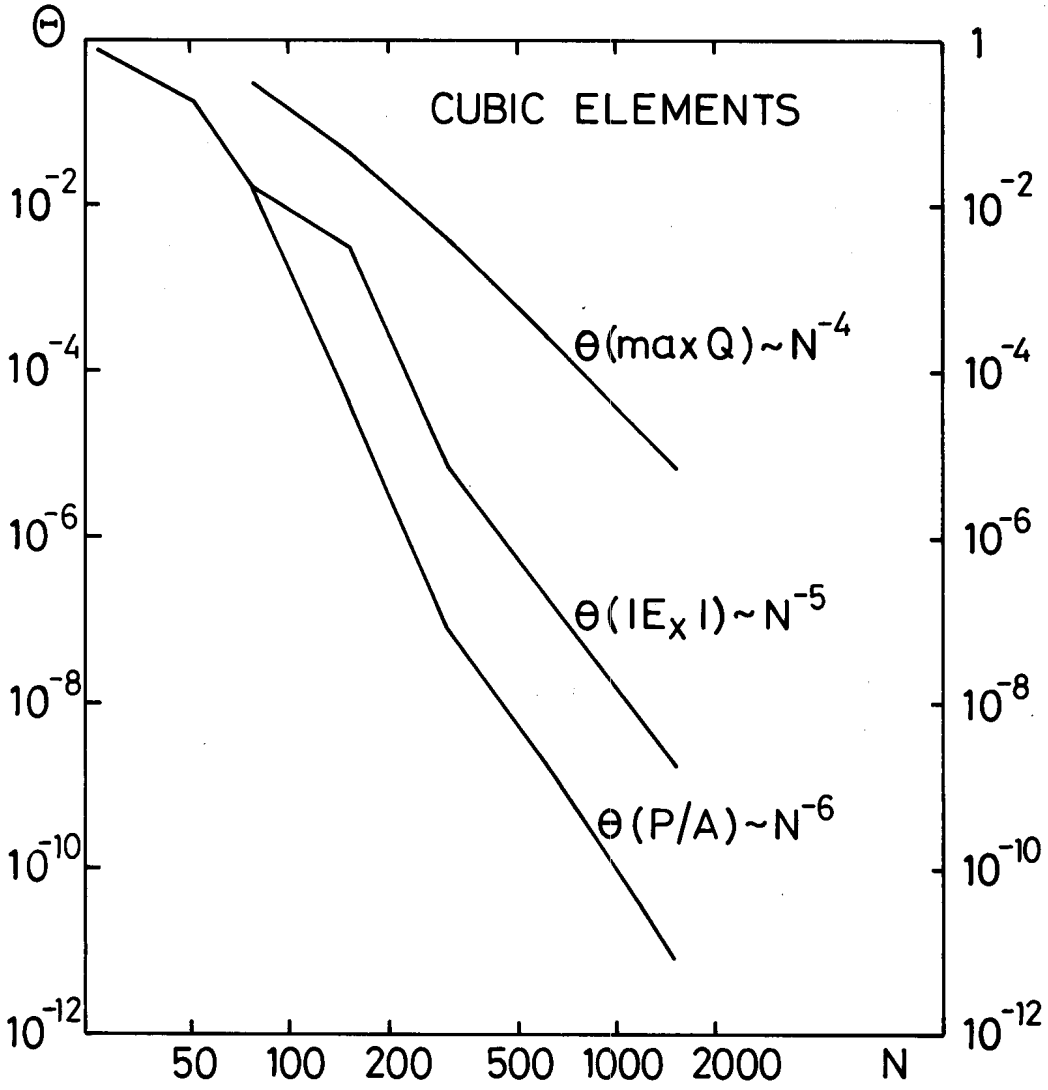
Θ
1
CUBIC ELEMENTS
10^{-2}
10^{-4}
10^{-6}
10^{-8}
10^{-10}
10^{-12}
$\theta(\max Q) \sim N^{-4}$
$\theta(|E_X|) \sim N^{-5}$
$\theta(P/A) \sim N^{-6}$
50
100
200
500
1000
2000
N

FIG. 10

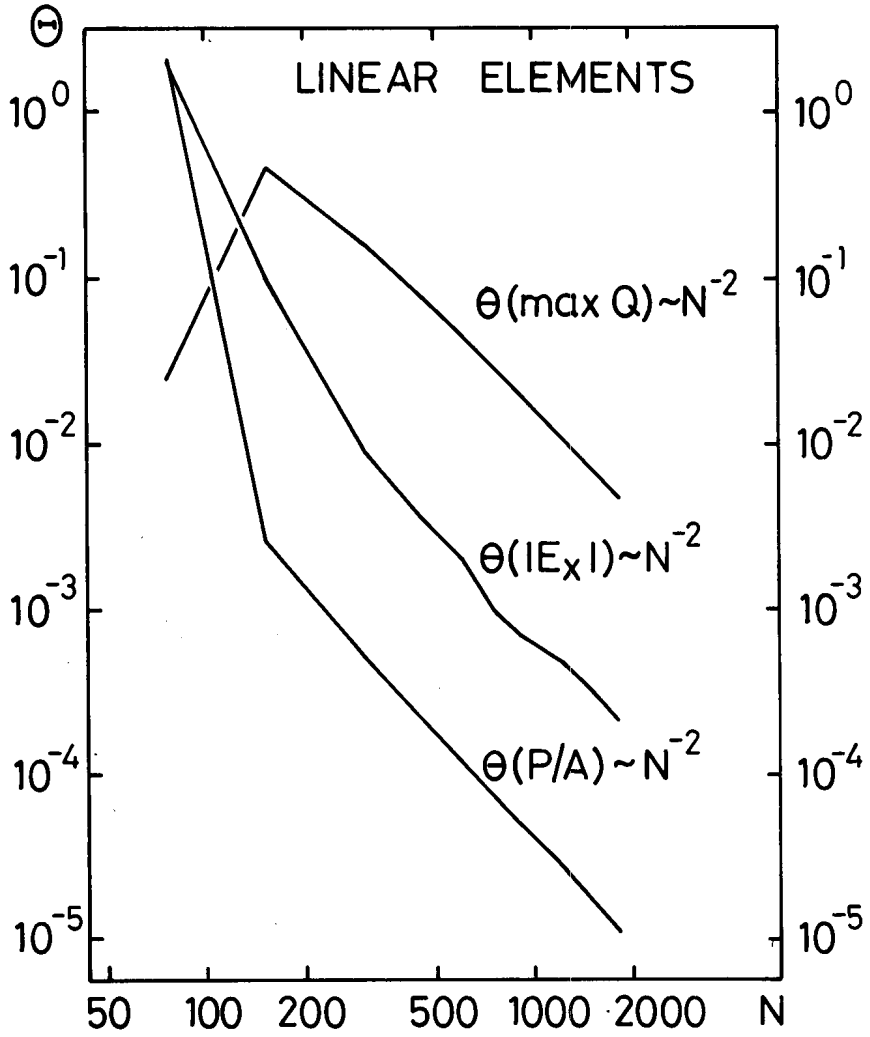
Θ
LINEAR ELEMENTS
10^0
10^{-1}
10^{-2}
10^{-3}
10^{-4}
10^{-5}
θ(max Q)~N^{-2}
θ(|E_x|)~N^{-2}
θ(P/A)~N^{-2}
50
100
200
500
1000
2000
N

FIG. 11

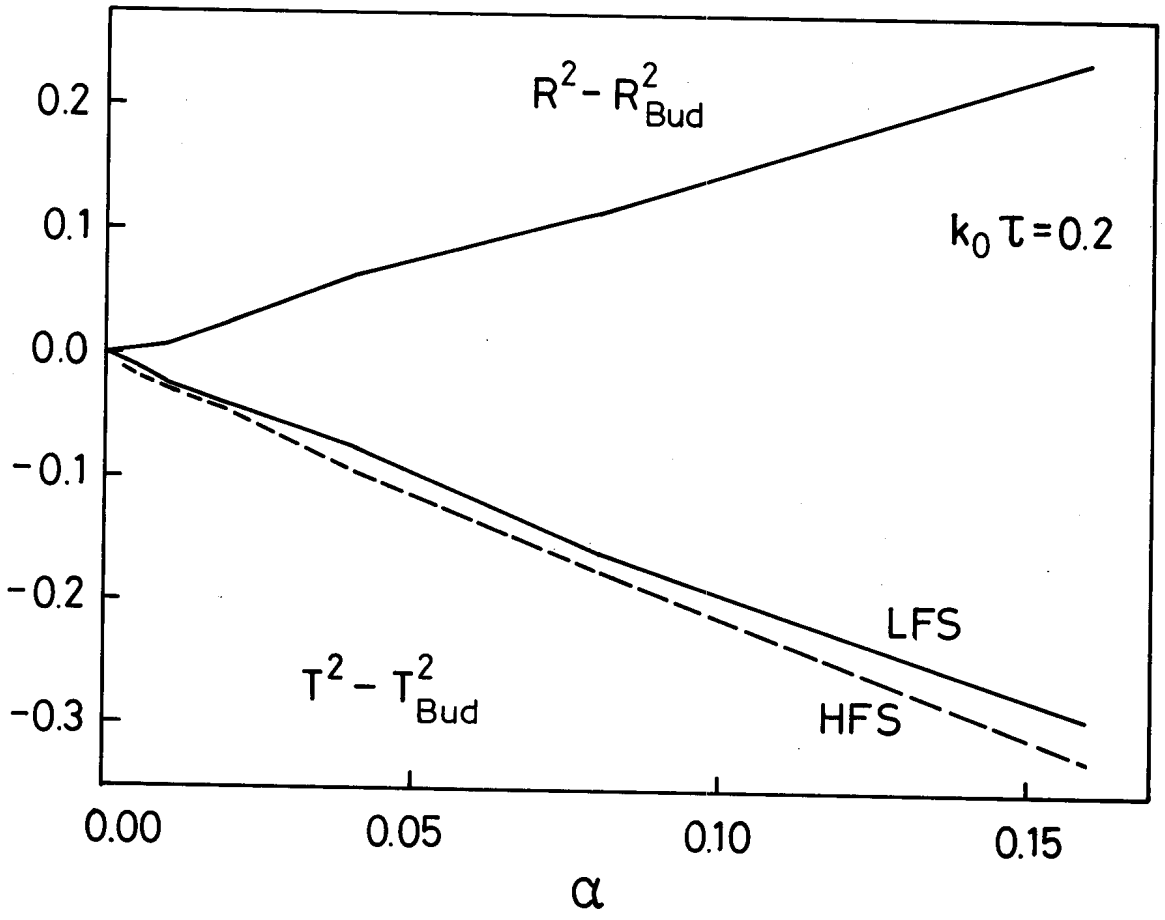
0.2
0.1
0.0
-0.1
-0.2
-0.3
$R^2 - R^2_{Bud}$
$k_0 \tau = 0.2$
LFS
HFS
$T^2 - T^2_{Bud}$
0.00
0.05
0.10
0.15
α

FIG. 12

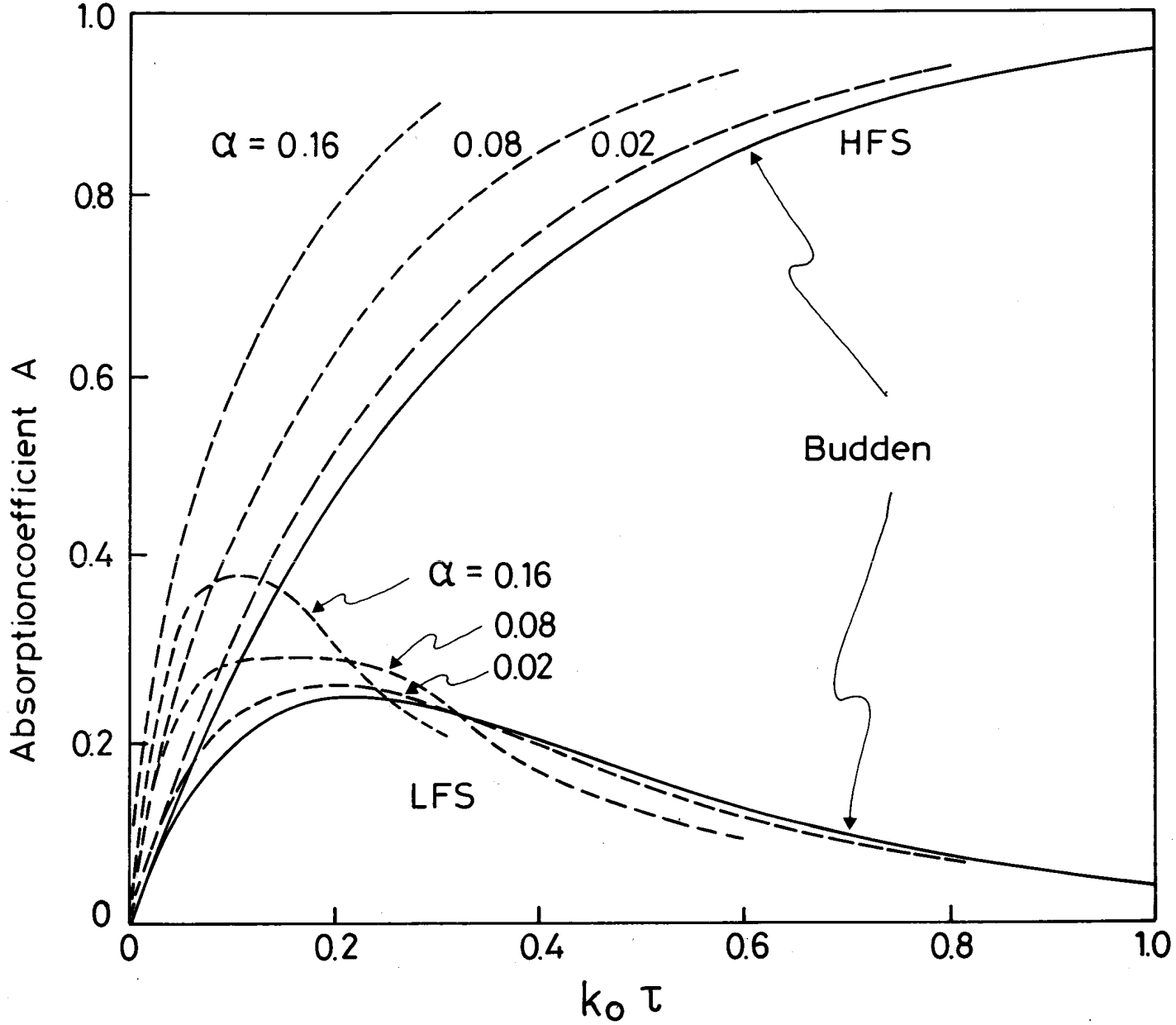
1.0
0.8
0.6
0.4
0.2
0
Absorptioncoefficient A
α = 0.16
0.08
0.02
HFS
Budden
α = 0.16
0.08
0.02
LFS
0
0.2
0.4
0.6
0.8
1.0
k₀ τ

FIG. 13

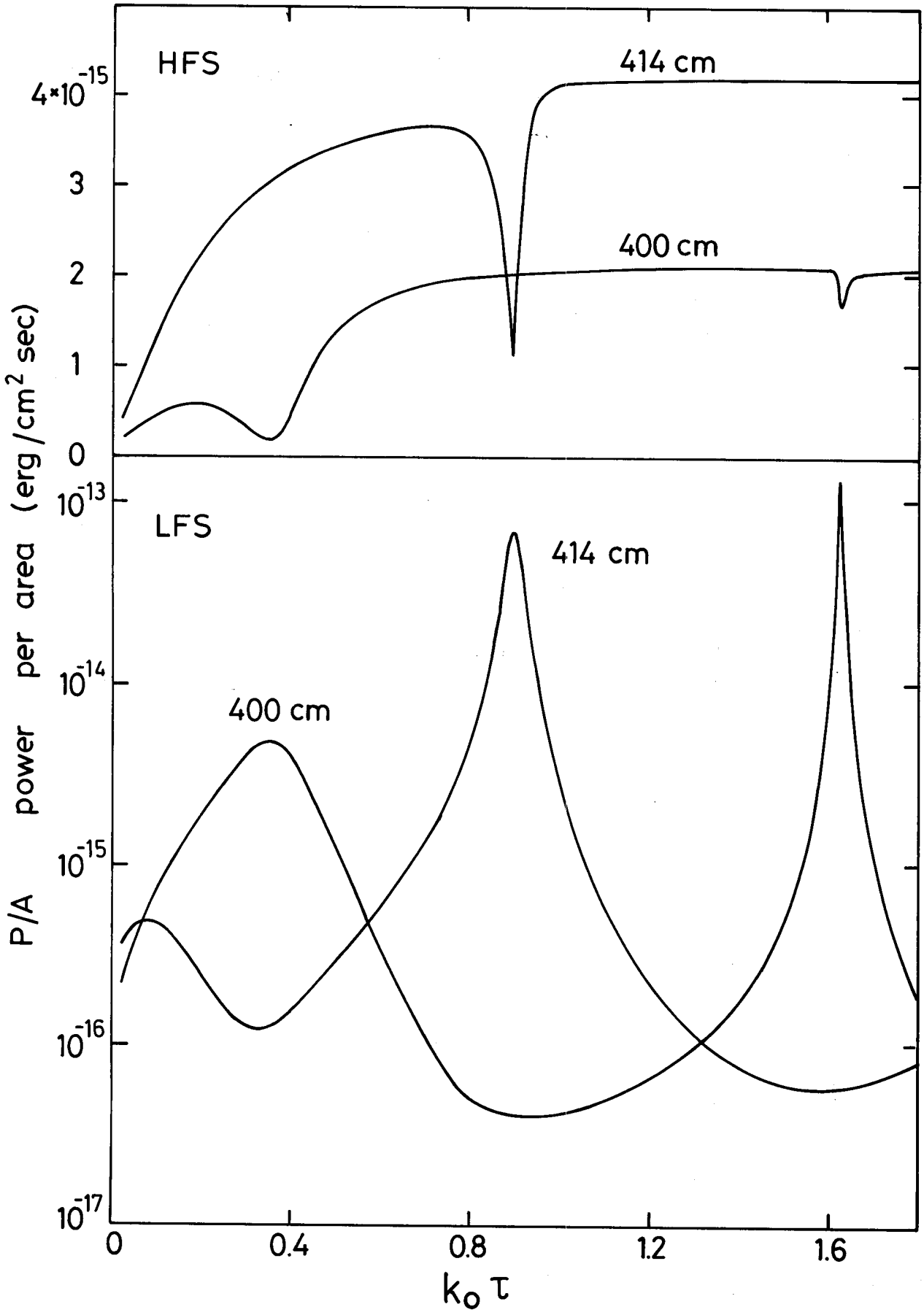
HFS
414 cm
400 cm
4×10⁻¹⁵
3
2
1
0
LFS
414 cm
400 cm
10⁻¹³
10⁻¹⁴
10⁻¹⁵
10⁻¹⁶
10⁻¹⁷
P/A power per area (erg/cm² sec)
0
0.4
0.8
1.2
1.6
k₀ τ

FIG. 14